Conceptual Design of a Non-Constant Leading-Edge Flying Wing UCAV Model

Hassan Aleisa* and Konstantinos Kontis†
University of Glasgow, Glasgow, G12 8QQ, UK

Berkay Pirlepeli‡ and Melike Nikbay§
Istanbul Technical University, Istanbul, 34469, Turkiye

The design of unmanned combat aerial vehicles (UCAVs) is primarily governed by the low-observability requirement for military applications rather than their aerodynamic performance. Conceptual design and optimization of UCAV models via size and shape variables for different missions in different flow regimes form a research area for military vehicle design. Flying wing UCAVs experience flow separation during takeoff and landing and furthermore exhibit stability issues. The aerodynamic performance of these UCAVs can be significantly improved by re-designing their leading-edge sweep angle and wing planform. In the present work, the initial weight determination, aerodynamic sizing, planform with and without inlet lip integration and then the conceptual design of a non-constant leading-edge flying wing UCAV configuration is performed. Next, the obtained conceptual design is 1:20 down-scaled to be used as a wind tunnel model and optimized for low-speed conditions using a Kriging-based surrogate model with a vortex-lattice method to maximize the lift-to-drag ratio. Later, the optimized design is validated using an open-source computational fluid dynamics (CFD) code, OpenFOAM 8.0, to verify the accuracy of the surrogate model and to investigate the aerodynamic characteristics. The optimized UCAV design exhibited improved aerodynamic characteristics in terms of lift-to-drag ratio. Furthermore, the aerodynamic performance and flowfield of the optimized UCAV model with and without inlet lip integration have been evaluated at low and high speeds.

Nomenclature

AOA	=	angle of attack [deg]
AR	=	wing aspect ratio [-]
b	=	wingspan [m]

*Postgraduate Researcher, Aerospace Engineering Department, AIAA Member.
†Professor, Aerospace Engineering Department, AIAA Fellow
‡MSc student, Computational Science and Engineering, Researcher AeroMDO Lab
§Professor, Aeronautics and Astronautics Engineering Department, Director AeroMDO Lab, AIAA Associate Fellow

C_D	=	wing drag coefficient [-]
C_L	=	wing lift coefficient [-]
C_p	=	pressure coefficient [-]
LE	=	leading edge [-]
Ma	=	Mach number [-]
P	=	pressure [N/m^2]
PS	=	pressure surface [-]
SS	=	suction surface [-]
TE	=	trailing Edge [-]
U	=	free-stream velocity [m/s]
u	=	local velocity [m/s]
X, Y, Z	=	coordinate axes
X	=	chordwise direction [m]
Y	=	spanwise direction [m]
Z	=	vertical direction [m]
$Y+$	=	non-dimensional wall distance [-]
Λ	=	sweep angle [deg]
k	=	turbulence kinetic energy [m^2/s^2]
ω	=	specific turbulence dissipation rate [1/s]
AVT	=	Applied Vehicle Technology
NATO/STO	=	North Atlantic Treaty Organization/Science and Technology Organization
SACCON	=	Stability And Control CONfiguration
MULDICON	=	MULti-DIsciplinary CONfiguration

I. Introduction

THE military forces have gained more confidence in deploying unmanned aircraft for actual combat missions since the early 1990s due to advancements in communication and automated systems. The primary role of the present unmanned aerial vehicles (UAVs) is to perform ISTAR (Intelligence, Surveillance, Target Acquisition, and Reconnaissance) missions which are critical for the military during combat scenarios [1]. The usage of UAVs in combat missions has gained momentum owing to their advantages, such as reduced human fatalities and suitability for 4d (dull, dirty, dangerous, and deep) missions, etc. The role of UAVs in combat missions includes surveillance, penetrating, suppressing enemy air defence systems, eliminating dangerous targets, etc. [2]. The stealth features are critical to overcoming the detection by enemy radars, thereby increasing the survivability of the UAVs in combat missions. Hence, reducing the radar cross-section (RCS) to very low levels such as -30 dB increases the survival chances of the aircraft because of the reduced detection range and insufficient reaction time of air defence systems [3]. However, armed UAVs with traditional configurations suffer from increased vulnerability to the enemy air defences due to the absence of stealth features [4]. Hence, designs with these configurations are unsuitable for operating in such hostile environments.

Modern classes of combat UAVs were developed as strike platforms with exterior weapon pylons such as the armed medium-altitude long-endurance (MALE) UAVs, MQ-9, or buried bomb bays such as Dassault nEUROn and Northrop Grumman's naval X-47B Unmanned Combat Aerial System (UCAS) (Fig.1). The main difference between the armed MALE UAVs and UCAVs is that the latter has increased speed and enhanced survivability due to its stealth design characteristics [5]. UCAVs are typically used for high-risk ground attack missions and they are relatively cheaper than their manned combat counterparts. However, they lack manned combat aircraft features such as supersonic cruise and higher manoeuvrability. The conceptual design of present UCAVs lies between the fighter and the bomber [6]. The UCAV configurations used in military applications must operate in a high-threat environment with sufficient operating range, endurance, and manoeuvrability which is appropriate for long-distance attacks, great depth, and stealth penetrations.

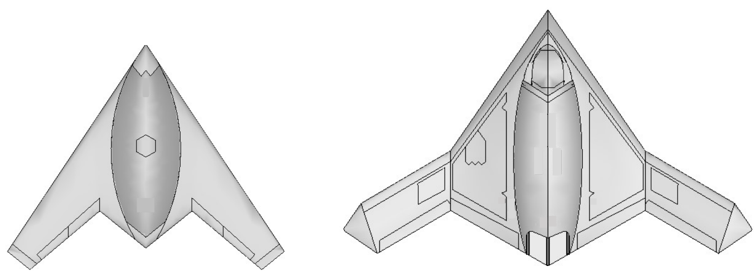

Fig. 1 Dassault nEUROn (left) and Northrop Grumman's naval X-47B (right) concepts.

Most of the UCAV conceptual designs available in the literature [7–20] are tailless flying wing configurations with a low to moderate aspect ratio (AR), internal weapon carriage, concealed propulsion systems, absence of high lift devices, and moderate to high leading-edge (LE) sweep angle edge-aligned wings ($40 \leq \Lambda \leq 60$ deg) [21, 22]. However, the design of UCAV configurations is a complex task because it requires a high level of integration within the subsystems combined with vorticial flow structures. Moreover, the flow around these configurations needs additional experimental and simulation investigations for verification [8, 23].

The typical lambda shape demonstrator configurations such as UCAV 1303, SACCON, and MULDICON were developed to investigate the aerodynamic characteristics. These design configurations corresponded to constant LE sweep variants such as Boeing Phantom Ray, Dassault nEUROn and BAE Taranis. The model 1303 UCAV was developed as a joint project between AFRL and Boeing, and it exhibited a typically blended flying wing-body (BWB) with ±47 deg LE sweep angle, ±30 deg trailing edge (TE) sweep, and a single crank [9]. This model was extensively investigated by various experimental and CFD analyses [9–13, 24].

Woolvin [12] presented a tradeoff study between UCAV configurations and their performance of model 1303 along with other configurations with LE sweep 30 and 60 deg, respectively. They reported that the parameters such as takeoff distance and mission radius were critical along with the sizing limitations, and the 30 deg configuration was heavier than the other two cases for the same mission radius. They concluded that the UCAV size was strongly influenced by the mission requirements, and the optimum tradeoff between them was crucial to utilize the full potential of the configurations with a better aerodynamic performance. Coppin [13] optimized the 1303 UCAV geometry using coupled adjoint and vortex lattice methods to reduce the drag at cruise while delaying the LE flow separation during takeoff. The optimized designs exhibited higher lift and better cruise characteristics; however, higher lift designs experience flow separation during the cruise.

NATO STO/AVT research task groups have been involved in developing experimental and CFD approaches to design and evaluate modern UCAVs. These works provide a deeper understanding of combat aircraft and UCAV design technologies, solve the technological challenges and help to develop new innovative ideas for next-generation combat aircraft and UCAV designs. Table 1 shows examples of AVT activities that contributed to combat aircraft and UCAV design and performance assessment. Generally, AVT research task groups cover core topics [17, 25] such as CFD methods and code validation [8, 14, 23, 26–28], the study of flow physics and aerodynamic characteristics [22, 29–32], predictions of stability and control (S&C) [8, 28, 33–36], design selection, specification, requirements and control ideas [37, 38], multidisciplinary design [15, 16, 18, 20], aeroacoustics [39, 40], infrared and radar signature [41, 42].

The SACCON conceptual configuration was developed with the help of the NATO STO/AVT-161 task group [14, 15, 23, 27, 43–46]. It is a highly swept (Λ =±53 deg) lambda wing UCAV model with parallel LE and TE [14, 23]. It was used to evaluate utilizing CFD to estimate the S&C characteristics of UCAVs. The research task group AVT-161 was later expanded by the task group NATO STO/AVT-201 to provide S&C databases for UCAV simulation and to predict the effects of the control surface [8, 28, 33, 35, 36, 46–49]. Liersch et al. [15] provided conceptual design analyses for the SACCON configuration and compared the aerodynamic performance of the SACCON model using low- and high-fidelity approaches.

The NATO STO/AVT-251 task group extended the works of AVT-161 and AVT-201 and re-designed the SACCON to develop a new configuration, MULDICON. It was designed to achieve specific mission requirements for UCAV configurations [16–20, 50]. Liersch et al. [17] provided a detailed review of the works of AVT-251 task group and the preceding task groups, AVT-161 and AVT-201, respectively. Five design teams of AVT-25 group were involved in the design of the MULDICON. A contribution to aerodynamic design included the effect of airfoil shape, LE geometry, engine integration, and the vortex flow at various angles of attack (AOA) on the aerodynamic characteristics of a 53 deg swept UCAV configuration by Schütte et al. [19]. A UCAV wing design and optimization process for the MULDICON

Table 1 Activities Contributed to Combat Aircraft and UCAV Design and Performance [25]

Activities	Year
VFE-2/ AVT-113 Understanding and Modeling Vortical Flows	2004 – 2007
X-31/ SACCON/ AVT-161 Assessment of Stability and Control Prediction Methods	2008 – 2011
AVT-183 Reliable Prediction of Separated Flow Onset and Progression	2010 – 2014
SACCON DLR-F17E/DLR-F19/ AVT-201 Reliable Stability & Control Prediction Methods for NATO Air Vehicles	2012 – 2014
AVT-232 IR signature prediction	2014 – 2016
AVT-233 Aeroacoustics of Engine Installation	2014 – 2017
AVT-239 Innovative Control effectors	2014 – 2017
Re-Design SACCON to MULDICON/ AVT-251 MD design agile NATO Air Vehicles	2015 – 2018
AVT-281 EO Signature Prediction	2017 – 2019
AVT-295 Demonstration of Innovative Control effectors	2017 – 2020
MULDICON/Fighter Aircraft/ AVT-316 Vortical Flow prediction and assessment	2018 – 2021
AVT-318 Low noise aeroacoustics design	2018 – 2021
AVT-307 Separated Flow Sym.	2019
AVT-324 MD Design RSM	2020
AVT-ET-205 Enhanced EO Prediction	2020 – 2021
AVT-366 Use of CFD for Design	2021
AVT-351 Enhanced Computational Perform. and S&C Pred.	2020 – 2023

UCAV was presented by Nangia et al. [20]. The MULDICON configuration is an improved version of the SACCON planform with the identical span and LE sweep angle. However, it exhibits a reduced TE sweep angle (30 deg) compared to the SACCON planform to enhance the aerodynamic performance of TE control surfaces [18, 19], as shown in Fig.2.

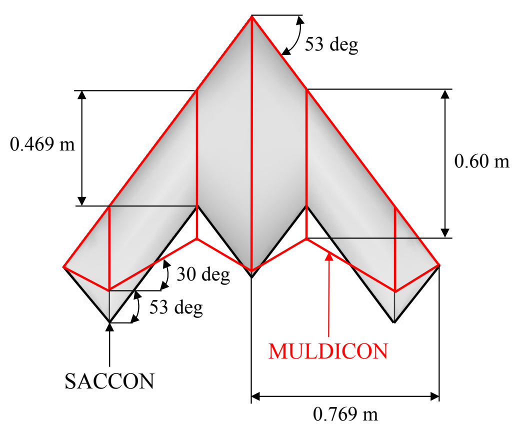

Fig. 2 Planform and geometric parameters of the SACCON and MULDICON configurations.

The above discussion shows that a single LE sweep angle design is insufficient to meet all UCAV design criteria. As the LE sweep angle reduces, the LE vortex strength increases, and vortex breakdown occurs at low AOA values. In contrast, the stall inception is delayed when it is increased, and the lift is enhanced at a higher AOA. Moreover, a wing with a high LE sweep angle is suitable for achieving high-speed cruise requirements. However, a higher LE sweep angle deteriorates aircraft controllability at low speeds [51].

The UCAVs are expected to operate in severe conditions with higher manoeuvrability and AOAs. Furthermore, the UCAVs may need to takeoff and land at aircraft carriers, and it is a challenging task because of the aerodynamic interaction between the UCAV and aircraft carriers. Northrop Grumman X-47B was the first UCAV to takeoff and land from an aircraft carrier [52]. It adopts a non-constant LE sweep angle design with 55/30 deg. The non-constant swept flying wing UCAVs configurations use high swept inboard and moderate swept outboard adopt to enhance the aerodynamic characteristics of UCAVs such as X-45A and X-47B.

Only a handful of literature is available to study non-constant LE sweep angle design, such as the experimental works of Manshadi et al. [53] and Yaniktepe et al. [54] etc. Extensive research has been performed on aerodynamic design and optimization of constant LE sweep wing models. However, there is less research into the non-constant LE sweep angle UCAV configurations. Furthermore, the non-constant LE sweep angle models exhibit complex mixed attached/ separated flowfields at the high lift, and this aerodynamic phenomenon has not been understood well. Hence it is required to perform an extensive study to understand their complex aerodynamic characteristics. The present study aims to provide a conceptual configuration of a non-constant LE flying wing with the initial sizing and then optimization procedure applied to the down-scaled wind tunnel model to enhance the aerodynamic performance. The flow field analyses of the optimized UCAV model are presented and studied to elucidate the flow characteristics of the flying wing UCAV model.

II. Initial Sizing

The preliminary aircraft sizing provides three fundamental parameters, including maximum takeoff weight ($W_{Takeoff}$), engine thrust (T_{Engine}), and wing reference area ($S_{Reference}$), which rule the size of aircraft, the complexity of calculations, and the manufacturing cost. The statistical data can be used to find out $W_{Takeoff}$, T_{Engine} and $S_{Reference}$ [5, 51, 55].

A. Typical UCAV Mission

Fig.3 illustrates a typical UCAV mission with several flight phases. A UCAV is used to accomplish ground strike-type tasks with cruise speeds from Mach number (Ma) = 0.7 to 0.85 [2, 3, 56]. The aircraft would operate out of an airfield during takeoff in some friendly territory. The length of the runway to some threshold altitude would be restricted, and it is critical for aircraft carrier operations. The air vehicle would climb with a high rate of climb and small fuel requirement to its cruising altitude of up to 11 km. Cruise phases should be at optimum speed and altitude to save fuel and desirable long-range. Then the aircraft would loiter for 1 hour at a lower altitude with desirable long-endurance to a location where it could use sensors and deploy its weapon. The dash phase occurs at low to moderate altitudes (0.1-5 km) for short distances with velocities equivalent to Ma = 0.9 and allowable combat acceleration manoeuvring up to 7.5

g to release weapons [3, 56]. On the way back to its base, it is essential to make air-refueling after 500 nautical miles (nm). The aircraft would loiter for 0.75 hours for air-refueling to be ready for any further combat requirements that might be needed, or it just would loiter in a friendly area. Then the aircraft would approach to lose altitude and slow its speed to land. Finally, it would touchdown and rest before the runway ended.

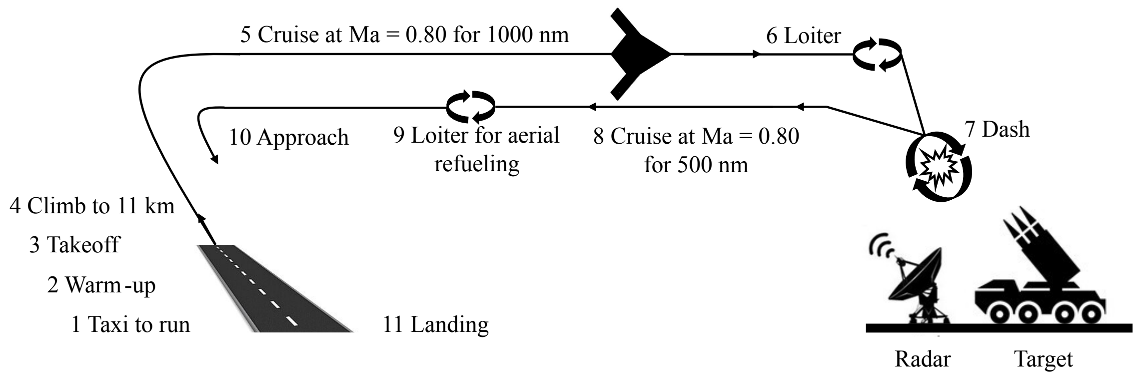

Fig. 3 Mission profile.

B. Analysis of weight

Combat UAV/UCAV is developed as a low observability strike platform with external weapon pylons or internal bomb bays and a takeoff weight of larger than 1000 kg [57]. In this work, the $W_{Takeoff}$ and T_{Engine} of UCAV are determined based on the statistical analysis. Design $W_{Takeoff}$ of aircraft is divided into various weights such as fuel (W_{Fuel}), payload ($W_{Payload}$), and empty (W_{Empty}), respectively. The W_{Empty} consists of parts such as the structure, propulsion systems, landing gear, airborne equipment/system, avionics etc. The $W_{Takeoff}$ is the summation of all weights on the aircraft at the takeoff phase, and Eq. (1) summarizes the takeoff weight buildup [5, 51, 58].

$$W_{Takeoff} = \sum_{i=0}^{max} W_i \tag{1}$$

1. Thrust-to-Takeoff Weight Ratio

The $W_{Takeoff}$ and T_{Engine} are critical design factors relating to aircraft preliminary sizing and can be obtained through the statistical data of comparable parameters of several present UCAVs. According to the statistical analysis of relevant weight data of existing UCAVs, Table 1 shows several types of UCAVs and the development of thrust-to-takeoff weight ratio ($T_{Engine}/W_{Takeoff}$) for X-45A/B/C and X-47A/B UCAVs, and their $T_{Engine}/W_{Takeoff}$ values are all reduced from the initial version to the latest version. Eventually, the UCAVs were developed from primarily air combat to ground attack due to increased endurance capability and some allowance for reduced manoeuvrability. The variation of the $T_{Engine}/W_{Takeoff}$ of several UCAVs is consistent with the differences in manoeuvrability, indicating that UCAVs' missions have shifted from air combat to ground attack nature as $T_{Engine}/W_{Takeoff}$ has changed. The bounds of

$T_{Engine}/W_{Takeoff}$ of UCAV are assumed initially as follows:

$$0.30 \leq T_{Engine}/W_{Takeoff} \leq 0.55 \tag{2}$$

Table 2 Weight data and engines types survey of UCAV [6, 56, 59–62]

UCAVs	$W_{Takeoff}$ ($10^3\ kg$)	$T_{Engine}/W_{Takeoff}$	**Engine type**	**Maximum** T_{Engine} (kN)
Boeing X-45A	5.5	0.55	Honeywell F124-GA-100	27.9
Boeing X-45B	9.7	0.49	General Electric F404-GE	48.9
Boeing X-45C	16.6	0.29	General Electric F404-GE	48.9
Northrop Grumman X-47A Pegasus	2.5	0.58	Pratt & Whitney Canada JT15D-5C	14.2
Northrop Grumman X-47B	20.2	0.36	Pratt & Whitney F100-220U	71.2
Dassault nEUROn	7	0.42	Rolls-Royce/Turboméca Adour Mk951	28.9
BAE Systems Taranis	8	0.37	Rolls-Royce/Turboméca Adour Mk951	28.9

Considering the design factors such as overall dimensions, fuel consumption, economic efficiency etc., therefore, the moderate-thrust turbofan engine would be selected as the propulsion unit for the UCAV. According to Eq. (2), the $T_{Engine}/W_{Takeoff}$ of UCAV is taken as an initial value of 0.40. The Honeywell F124-GA-100 turbofan engine with medium thrust was selected to power the aircraft based on the single-engine configuration. Hence, the maximum $W_{Takeoff}$ is 7000 kg.

2. The Total Fuel Weight Fraction for a Mission

The initial estimation for the weight components was obtained using the statistical coefficients excluding the fuel weight. The duration performance level was preliminary computed according to engine performance data [5, 58, 59]. The Phase Weight Fraction (PWF) is obtained using the fuel weight ratio to the $W_{Takeoff}$ of the aircraft. The mission profile comprises various phases and each phase uses fuel that adds up to the total fuel consumption (Table 3). The total PWF for a mission can be computed by Eq. (3)

$$PWF_{Total} = 1 - \prod_{i=1}^{N}(1 - PWF_i) \tag{3}$$

Where N is the number of mission phases and PWF_i is the fuel weight fraction for each phase.

Hence the fuel weight (W_{Fuel}) is computed by Eq. (4)

$$W_{Fuel} = PWF_{Total} \cdot W_{Takeoff} \tag{4}$$

Table 3 Fuel fraction

	Phase	Fuel Fraction
1	Runway, W_1/W_{TO}	0.990
2	Taxi, W_2/W_1	0.990
3	Takeoff, W_3/W_2	0.990
4	Climb, W_4/W_3	0.978
5	Cruise for departure, W_5/W_4	0.880
6	Loiter over target, W_6/W_5	0.955
7	Dash, W_7/W_6	0.985
8	Cruise to return, W_8/W_7	0.938
9	Loiter for refueling, W_9/W_8	0.966
10	Approach, W_{10}/W_9	0.990
11	Landing, W_{11}/W_{10}	0.995

The total fuel weight for the mission is initially computed as $W_{Fuel} = 2100\ kg$.

3. Payload

The payloads must be internally mounted and designed for the limited space of the weapons bay due to the low observability restriction. The small diameter bombs with a mass of approximately 100 to 500 kg such as GBU-16, EGBU-16, GBU-32, GBU-38 and GBU-39 and GBU-55 are typical for miniaturized air-to-ground missiles and bombs that are adapted to the concealed armament UCAVs. Payloads vary from 400 up to 2000 kg [6, 56, 59], and thus the payload weight ($W_{Payload}$) of UCAV is initially kept as 1050 kg.

4. Empty Weight

The UCAV was conceptually designed during the preliminary design process; therefore, there are no defined geometry or dimensions. As a result, it is necessary to benefit from available information for the aircraft according to the mission type. Typically, the empty weight fraction ($W_{Empty}/W_{Takeoff}$) can be from 0.2 to 0.75 [51]. Table 4 shows the $W_{Empty}/W_{Takeoff}$ ratio for several UCAVs, varying from 0.45 to 0.70. Therefore, the $W_{Empty}/W_{Takeoff}$ is assumed to be 0.55. The empty weight W_{Empty} can be calculated using Eq. (5)

$$W_{Empty} = W_{Takeoff} - W_{Fuel} - W_{Payload} \tag{5}$$

Table 4 Relation between $W_{Takeoff}$ and W_{Empty} of existing UCAVs [56, 59, 63]

UCAV	$W_{Empty}/W_{Takeoff}$
Boeing X-45A	0.600
Boeing X-45B	0.655
Boeing X-45C	0.489
Northrop Grumman X-47A Pegasus	0.698
Northrop Grumman X-47B	0.449

C. Aerodynamic Sizing

For UCAV configurations, it is a challenge to achieve a higher lift-to-drag (C_L/C_D) value for a small to moderate aspect ratio (AR). Furthermore, the low observability characteristics increase the difficulty in the UCAV conceptual design. The sweep angles of the UCAV planform can be changed to provide a group of comparable UCAV configurations. Varying the sweep angles substantially impacts the stealth characteristics, aerodynamics performance, stability and control, overall size, and cost. Hence, the UCAV configuration is selected based on RCS, aerodynamic characteristics, structural and packing constraints, and a trade-off of these aspects. Low observable aircraft have edge-aligned planforms with sweep angles $\pm\Lambda$ conforming to the signature requirements of the UCAV. A high sweep angle is desirable for minimizing RCS effects and incorporating the propulsion system. Moreover, a small wingspan is advantageous for logistical reasons, storage, and structural weight reduction. However, this impacts the AR, which influences the produced drag where a large AR is more desirable.

At low subsonic conditions, LE sweep angles of the wing decrease the maximum attached flow lift coefficient because an airfoil on a swept wing cannot maintain a high sectional lift, and the three-dimensional (3D) reduces the wing's performance [13, 64, 65]. The NACA 6-series airfoils can retain the laminar flow for a larger part of the chord length; consequently, they exhibit a relatively lesser minimum drag coefficient ($C_{D_{min}}$) than the NACA 4 and 5 series [51]. The performance of UCAVs airfoils is analyzed to obtain lift, drag polars, $C_{l_{max}}$ and C_l/C_d at a range of typical chord Reynolds (Re) number between $5 \cdot 10^6$ and $2 \cdot 10^7$ [5]. The C_L initial sizing for a wing of the finite span was computed by the classical approach [58, 64], where the maximum lift coefficient ($C_{L_{max}}$) is determined by averaging the $C_{L_{max}}$ of the wing tip and wing root, corrected for 3D of the wing flow and quarter chord sweep, using Eq. (6)

$$C_{L_{max}} = 0.9 \cdot C_{L_{max}} \cdot \cos\Lambda_{0.25} \tag{6}$$

Estimates of the planform area were performed [58, 65]. The average wing-loading of other UCAVs is about 121 kg/m^2; therefore, the wing area is 58 m^2. The drag coefficient using (Eq. (7)) sizing can be calculated using the simplified assumption that the C_{Dmin} is equivalent to the zero-lift drag coefficient (C_{D0}) [5, 51]. The initial estimation for C_{D0} was derived from the literature [5, 51, 58] and it must be noted that it is a statistical value rather than based on a specific configuration. The C_{D0} of the final design should be less than this initial value for an aerodynamically efficient UCAV configuration. For initial sizing purposes, the span efficiency factor (e) was estimated to be 0.65.

$$C_D = C_{D0} + \frac{C_L^2}{\pi} \tag{7}$$

D. Conceptual Configurations

During planform selection, the X-series of UCAV (Fig.4) are considered in this study. Generally, these planforms consist of the tip, outer, and inner wing sections. The planform of X-45A/B shows that the LE sweep is fixed from centerline to tip at 45 deg. The configuration is characterized by an extended forward central fuselage strake region and a uniform chord outboard wing. Considering the X-47B shape, X-47B is a slightly pudgy part with the nature of typical airframe features [66].

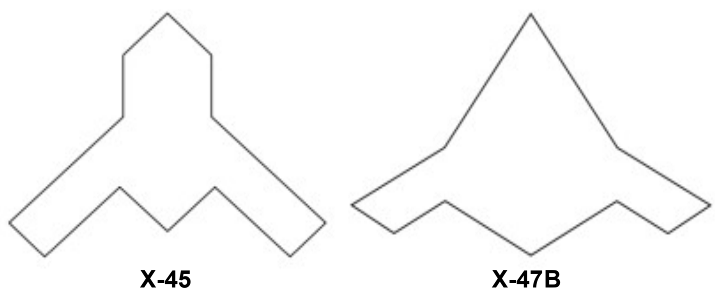

Fig. 4 Non constant LE sweep UCAV Planforms.

The low observable edge-aligned aircraft intakes are top-mounted and integrated with the aircraft forepart to conceal them and reduce RCS effects [13, 67]. The inlet designs take different lip-plane shapes, such as the V-shaped inlet for X-45A and X-47B and the W-shaped inlet for nEUROn. In this study, the inlet lip plane has a V-shaped inlet with rounded edges to improve meshing and minimize flow separation. The geometrical parameters for the inlet lip plane include the contraction ratio ($CR = A_{highlight}/A_{throat}$), which governs the lip thickness to enhance pressure recovery, reducing separated flow at the inlet entrance. The CR value generally varies from 1.05 to 1.20; a lower value indicates a sharp lip which is suitable for high-speed applications whereas a higher value indicates an elliptical lip that is suitable for low-speed and high AOA values [68]. The $A_{highlight}$ and A_{throat} can be estimated by the isentropic relations (Freuler's approach [69], the 1-D isentropic Area-Mach relation) and using the engine fan starting section (aerodynamic interface plane (AIP)). The inlet capture area ($A_{capture}$) is approximately 0.4918 m^2.

Baals et al. [70] and Nichols et al. [71] provided a detailed study of the effect of inlet lip geometry on aerodynamic performance. They reported that the NACA 1-series airfoils provide good performance by delaying sonic and separated flow for a large span of duct-to-flight-velocity ratios and Ma numbers [70–73]. Furthermore, Re [74] studied the aerodynamic performance of various NACA 1-series inlets and concluded that the inlet critical Ma number depends on the lip shape [74, 75]. NACA 1-81-100 series (Fig.5) is used for lip profile, and the normalized dimensions of NACA 1-81-100 series [74–76] are used to develop lip geometry.

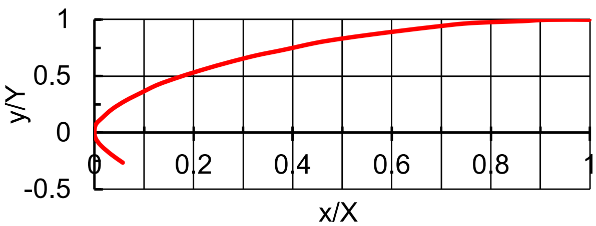

Fig. 5 NACA 1-81-100 airfoil.

Fig.6 shows the 3D view of the present UCAV. Table 5 shows a comparative of configuration parameters for X-45A, X-47B and the present UCAV. In this UCAV design, the aircraft shape adopts a blended flying wing plus a non-constant LE sweep angle concept because it allows planform optimization. Both fuselage and wing sections are generated by using NACA 64_1212 airfoil profile. Moreover, its superior lift-drag characteristics aid in satisfying the C_L/C_D ratio requirements and achieving the UCAV's performance objectives.

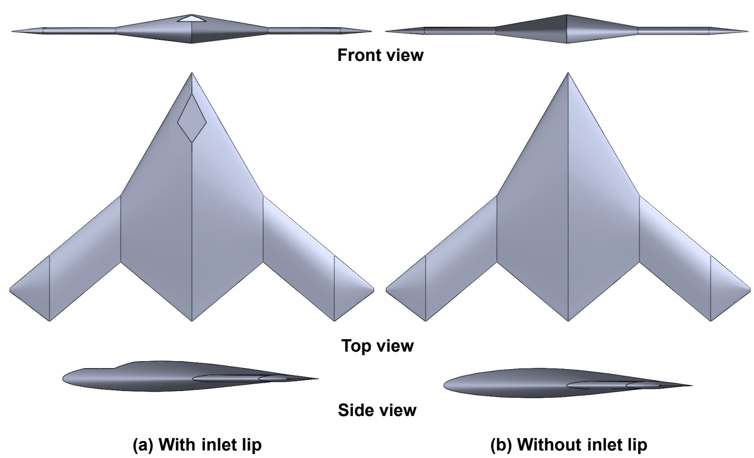

Fig. 6 Present UCAV's 3D views.

III. Design Optimization of a Scaled-Down UCAV Configuration

Our research team plans to perform some experimental studies at the University of Glasgow De Havilland Wind Tunnel in the next phase of the project to investigate the aerodynamic characteristics of non-constant LE-swept UCAVs and to validate computational results. For this reason, based on the conceptual design performed in the previous section, a 1:20 scaled-down UCAV model is generated to be used in the experiments later. Before manufacturing the experimental UCAV model, a preliminary design optimization study is performed to improve the scaled-down UCAV

Table 5 Conceptual configuration parameters

Parameters	X-45A	X-47B	Present UCAV
Wing Span,b, $[m]$	10.31	18.9	15
Length of Fuselage, l_f, $[m]$	8.08	11.63	10
LE inboard sweep angle, Λ_{LEI}, $[deg]$	45	55	60
LE outboard sweep angle, Λ_{LEO}, $[deg]$	45	30	40
TE sweep angle, Λ_{TE}, $[deg]$	45	30	40
Aspect Ratio, AR $[-]$	3.23	4.24	3.629
Span/fuselage length ratio, (b/l_f) $[-]$	1.28	1.626	1.428
Airfoil profile, $[-]$			NACA 64_1212

model for the flight conditions implied by the wind tunnel. The wind tunnel has a test section of 2.65 m · 2.1 m · 5.4 m with a maximum speed and Re number of 70 m/s and $4 \cdot 10^6$, respectively. The experimental UCAV model will be tested at 30 m/s. The UCAV model will be manufactured using FDM 3D printer with a maximum part size of the 400 · 400 · 350 mm working envelope, so the span of the experimental UCAV model is limited by 0.75 m.

The aerodynamic performance of UCAV configurations relies heavily on the LE sweep angles of the swept wings. Therefore, the present optimization aims to improve the lift-drag ratio using design parameters such as including LE inboard sweep angle (Λ_{LEI}) and LE outboard sweep angle (Λ_{LEO}). In contrast, both the inboard and outboard TE sweep angles (Λ_{TE}) were kept fixed to maintain a fixed span (b). For the flow conditions, the incompressible flow assumption is made since the Ma number is in the subsonic range, Ma = 0.087 with Re number = 10^6, and altitude, h = 0 m. The baseline wing is composed of three parts which are the fuselage, the mid-section and the tip-section. While TE sweep angles are fixed, 40 deg for all three sections, initial LE sweep angles are 60, 40, 40 deg for each section respectively. The dimension of the planar wing are given in Table 6 and in Fig.7. NACA 64_1212 airfoil is used along the span which is kept fixed during the optimization.

Table 6 Baseline Geometry Dimension

Parameter	Description	Value
S, $[m^2]$	Wing Area	0.155
b, $[m]$	Wing Span	0.75
l_f, $[m]$	Length of Fuselage	0.525
c, $[m]$	Wing Root Chord	0.116
Λ_{LEI}, $[deg]$	LE inboard sweep angle	60
Λ_{LEO}, $[deg]$	LE outboard sweep angle	40

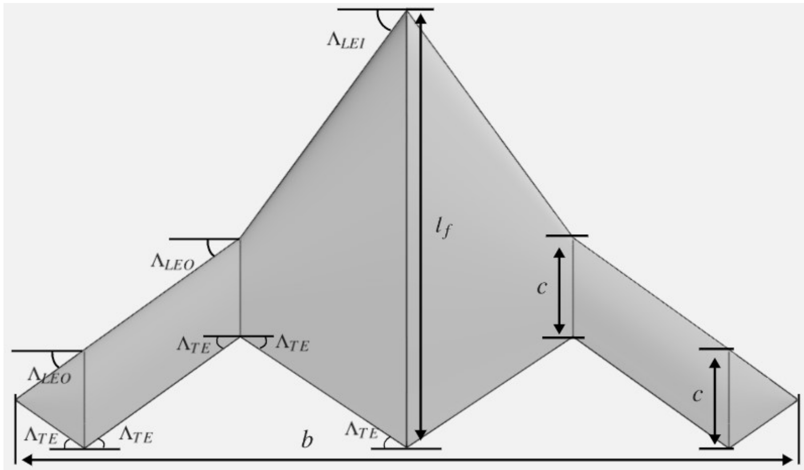

Fig. 7 LE sweep angles optimization.

A preliminary design optimization study is performed using the Kriging surrogate modelling with the linear vortex lattice method as a flow solver with the aim of decreasing the computational time of the optimization process before the test model will be manufactured. The constrained optimization problem is solved with a derivative-free genetic algorithm using Pymoo [77] which is an open-source multi-objective optimization code written in Python. The mathematical formulation of the optimization problem can be seen in Eq. (8).

$$
\begin{aligned}
\underset{\Lambda_{LEI},\Lambda_{LEO}}{\text{minimize}} \quad & f_1(s) = \frac{C_D(s)}{C_L(s)}, \quad f_2(s) = \frac{b}{\sqrt(S)} \\
\text{subject to} \quad & h_1(s) = \frac{b}{b_{ref}} - 1 = 0, \\
, \qquad & h_2(s) = \frac{l_f}{l_{fref}} - 1 = 0, \\
& s = \{\Lambda_{LEI}, \Lambda_{LEO}\}
\end{aligned}
\tag{8}
$$

Where b is the wingspan, l_f is the length of the fuselage at the root, and S is the wing area. b_{ref} and l_{fref} are 0.75 m and 0.525 m respectively.

To perform the optimization, the aerodynamic performance of variable wing designs is evaluated using a linear vortex lattice method (VLM) solver called VSPAERO developed by David Kinney at NASA Ames Research Center [78]. This method assumes that the flow is incompressible and inviscid, and neglects the thickness of the geometry. The grid is generated on the reduced planform geometry which is obtained from the 3D model. The wing surfaces are divided into 53 panels in a chordwise direction and 29 panels in a spanwise direction with leading-edge clustering of 0.25 and trailing-edge clustering of 0.05. The parametric nonplanar wing model is generated with a parametric vehicle design generation tool, OpenVSP, which was developed by NASA Langley Research Center [79]. The design variables are provided in Table 7.

Table 7 Optimization Parameters

Parameters	Description	Interval [deg]	Initial value [deg]
Λ_{LEI}, $[deg]$	LE inboard sweep angle	[50, 60]	60
Λ_{LEO}, $[deg]$	LE outboard sweep angle	[30, 50]	40

The surrogate model is constructed using the sample set generated with the Latin hypercube sampling (LHS) method. This technique divides the range of each design variable into several of samples and then generates randomly selected samples such that each sample will reside in one of the divided zones inside the range of the design variables in OpenVSP [80]. The number of the initial sample set is incremented such that the stratification of the design space in the initial set is maintained. After evaluating objective functions, the generated data is used to create the Kriging surrogate model. A total of 150 design points are evaluated with the low-fidelity analysis. The surrogate models for C_L/C_D were cross-validated with ten percent of the results with the errors reported in Table 8.

Table 8 Surrogate model error for C_L/C_D and $b/\sqrt{S}$

Quality metric	C_L/C_D	$b/\sqrt{S}$
Root mean squared (Training Points)	$1.2090 \cdot 10^{-14}$	$4.0087 \cdot 10^{-14}$
Root mean squared (Test Points)	$1.4064 \cdot 10^{-06}$	$3.6504 \cdot 10^{-05}$

The constrained optimization problem is solved by using a fast and elitist nondominated sorting genetic algorithm (NSGA2) method, which is a multi-objective genetic optimization algorithm [81]. Table 9 shows the comparison of the objective functions for the initial and optimized wings. Approximately a 1.3 percent increase in the lift-over-drag ratio compared to the original wing is obtained using only low-fidelity aerodynamic analysis. The final parameters are found to be Λ_{LEI} = 58 deg and Λ_{LEO} = 40 deg. A comparison between baseline and optimized geometry can be seen in Fig. 8. The overlap is represented by the shaded area. Finally, a CFD RANS analysis is performed for the optimal UCAV design to demonstrate the improvement in C_L/C_D values. The difference in C_L/C_D using the VLM low-fidelity solver and the CFD RANS solver is 8.47%; the high difference between the models is possibly due to the inviscid assumption of the VLM. C_L values are 0.3761 and 0.2958 for the baseline and optimized model respectively.

Table 9 Optimization results

Configurations	C_L/C_D (Low fidelity VLM)	C_L/C_D (High fidelity CFD RANS)
Baseline	4.8221	5.0177
Optimized	4.8868	5.3393
Improvement [%]	1.3	6.03

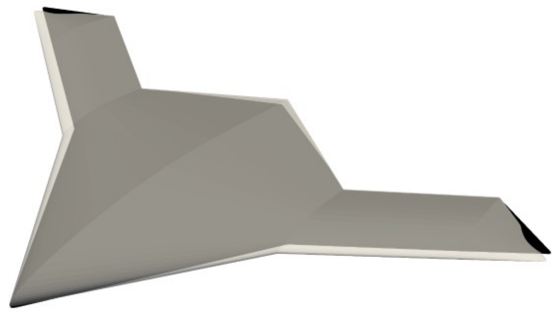

Fig. 8 Comparison between baseline wing geometry in black and optimized wing geometry in white.

IV. High-Fidelity Numerical Methodology

A. Model Geometry and Flow Domain

From now on, the optimum design determined for the 1:20 scaled UCAV model is employed in the present CFD analysis using OpenFOAM 8.0 [82] to predict the aerodynamic characteristics of the UCAV configuration. A 3D water-tight computer-aided design (CAD) model is produced using the CAD modeler Solidworks [83]. The geometrical specifications of the UCAV model used in the numerical analyses are shown in Table 10. The present UCAV model uses NACA 641212 airfoil profile for the wing profile. The top and side views of the present 3D model are shown in Fig.9.

Table 10 Geometrical specifications

Parameters	Λ_{LEI}**, [deg]**	Λ_{LEO}**, [deg]**	Λ_{TE}**, [deg]**	**S, [m^2]**	**AR [-]**
Values	58	40	40	0.145	3.87

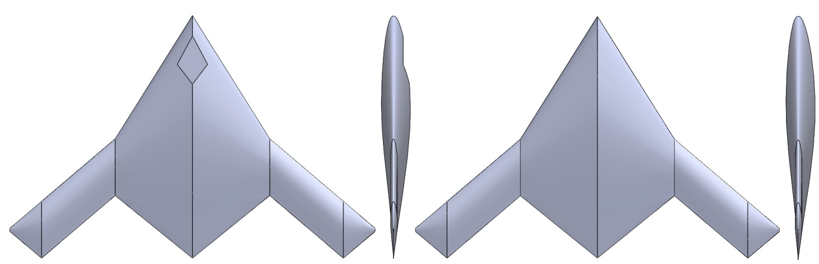

Fig. 9 Top and side views of the UCAV model with and without inlet lip.

A virtual wind tunnel with minimum and maximum bounds of (-2.4 0 -2.4) m and (5.4 2.4 2.4) m, respectively is used. The UCAV model is placed such that the origin lies at the TE. The flow along the x-, y-, and z-axes is considered as streamwise, spanwise, and thickness directions, respectively. Later, to extract the flow domain, the UCAV model is subtracted from the virtual wind tunnel and then exported as neutral formats such as Standard for the Exchange of Product Data (STEP) and Stereolithography (STL). The computational flow domain comprises the half-wing model with a symmetry plane to save computational power. Fig.10 shows the computational domain used in the present study.

The UCAV wing model is rotated in the y-axis to obtain the desired AOA values (0 to 40 deg), and no changes were made to the virtual wind tunnel.

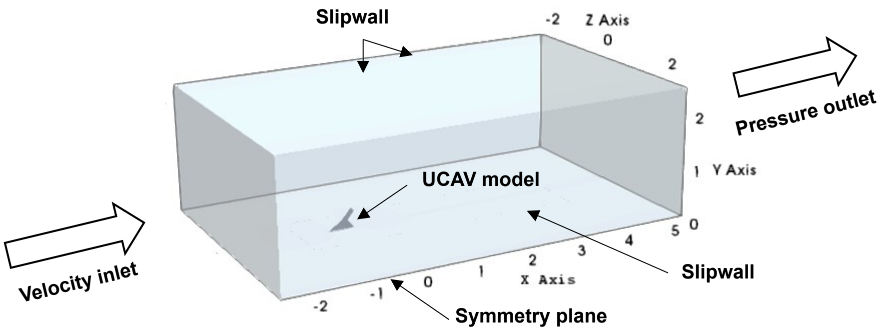

Fig. 10   Computational flow domain.

B. Grid Generation

Fig.11 provides the procedure used in the generation of mesh. The computational domain is discretized with the mesh generation libraries blockMesh and snappyHexMesh [82, 84, 85]. The blockMesh creates the hexahedral background mesh for the domain, and the snappyHexMesh is used to adapt the UCAV model into the computational domain.

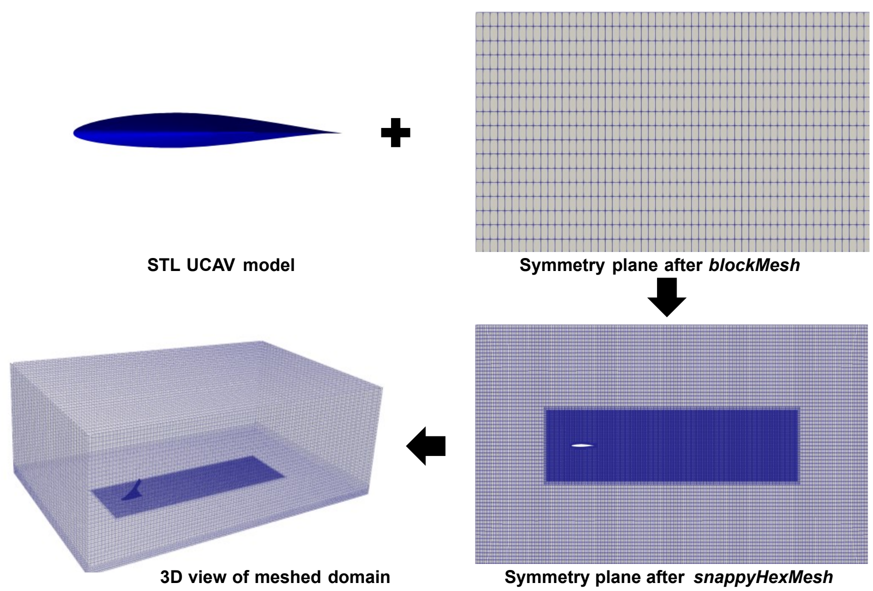

Fig. 11   The process of the mesh generation.

The blockMesh uses bound values identical to the computational domain, and the domain is divided into 30 cells in the x-direction and 15 cells in the y-and z-directions to create the background mesh. The background mesh consists of fully structured 15895 hexahedral cells. The snappyHexMesh embeds the UCAV wing model into the background mesh. It produces polyhedral cells during the integration process, and owing to its operating principle, it produces hex-dominant unstructured mesh.

In the present mesh, a careful approach is used to capture both near-wall and wake phenomena using the prism layers and a volumetric refinement box. The present mesh is generated to satisfy the requirements of the k-ω shear stress transport (SST) model to resolve the viscous sublayer region. To capture the near-wall effects, 10 prism layers with a layer expansion ratio of 1.05 (Fig.12) are used. The suction surface (SS) y+ distribution for the UCAV model is shown in Fig.13. As shown in the figure, the y+ value is less than 1 for a majority of the wing model, excluding LE and TE. Moreover, the average y+ value of the model is $\leq$ 1, which is sufficient to resolve the viscous sub-layer region.

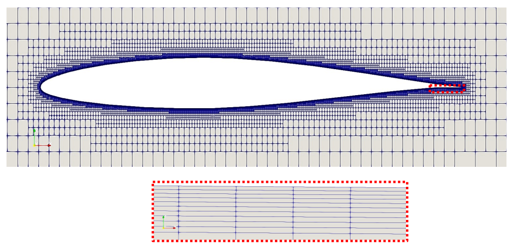

Fig. 12 The view of grids and prism layers on the models using SnappyHexMesh.

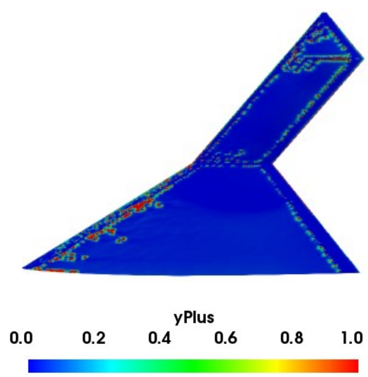

Fig. 13 SS y+ distribution for Top view of the UCAV model at AOA =20 deg.

C. Mesh Quality

It is essential to ensure that the mesh quality is adequately better to obtain accurate results. Generally, the quality of a mesh can be expressed in terms of critical parameters like non-orthogonality, skewness and aspect ratio etc. The mesh quality is obtained by running the command checkMesh in the terminal. The maximum and average non-orthogonality values for the present mesh are 64.97 deg and 9.24 deg, respectively. The maximum permissible value of non-orthogonality is 70 deg; since the present mesh has less non-orthogonality it is adequate to perform the flow analysis. Furthermore, the maximum skewness and aspect ratio were obtained as 3.67 and 24.96, respectively. As these values are within acceptable limits, it was concluded that the quality of the present mesh is sufficient to perform the aerodynamic analysis of the UCAV model.

D. Solver and Turbulence Model Selection

The present flow problem is steady and incompressible at low speed, and the simpleFoam solver is selected [82, 84]. The pressure-velocity coupling is attained through the Semi-Implicit Approach for Pressure-Linked Equations Consistent (SIMPLEC) algorithm. In contrast, the flow problem is steady and compressible at high speed, and the rhoSimpleFoam solver is selected [82, 84]. The under-relaxation factors are used to improve the convergence of the simulation. In the present study, the pressure and density are under-relaxed by values of 0.3 and 0.01, respectively, whereas all other variables are under-relaxed by a value of 0.7. Furthermore, the residual convergence criteria are set 10^{-6}. The two-equation k-ω SST model is chosen for the turbulence closure. It uses the k-ω SST model in the near wall zone and the k-ϵ model in the faraway region from the wall, and it is appropriate for the flows with separation and adverse pressure gradient. Many researchers have successfully used the k-ω SST model to predict the aerodynamic characteristics of the UCAV model [86–90]. Furthermore, second-order accurate schemes are used for spatial discretization.

E. Boundary and Initial Conditions

To obtain accurate results, appropriate initial and boundary conditions should be given. In OpenFOAM, the details of the initial and boundary conditions are given in the directory folder [84]. The present study assumes a low turbulence intensity $\leq$ 1% and uniform axial low (Ma = 0.087) as well as high speed (Ma = 0.80) at the inlet. A zero-pressure gradient condition is imposed at the outlet, and the far-field walls that are located away from the UCAV model are fixed as a slip boundary condition (zero shear stress). Lastly, the UCAV model is a no-slip wall. To calculate the initial conditions of the turbulence variables, the below equations Eq. (9) and Eq. (10) are used. For low speed, the initial values for the turbulence kinetic energy (k) and specific dissipation rate (ω) are 0.135 m^2/s^2 and 4500 $1/s$, respectively. For high speed, the initial values for the turbulence kinetic energy (k) and specific dissipation rate (ω) are 0.11 m^2/s^2 and 3700 $1/s$, respectively. Whereas the viscosity ratio μ_t/μ is taken as 2.

$$k = 1.5 \cdot (UI)^2 \tag{9}$$

$$\omega = (\rho k/\mu) \cdot (\mu_t/\mu)^{-1} \tag{10}$$

V. Results and Discussion

A. Grid Refinement Study

To evaluate the influence of grid resolution on the aerodynamic characteristics of the UCAV model, four grids with resolutions such as very fine (4.570 million), fine (3.315 million), medium (2.173 million) and coarse (1.168 million) are produced, and the C_L/C_D at 20 deg AOA is compared. Fig.14 shows the variation of C_L/C_D with increasing grid resolution. As shown in the figure, the variation of C_L/C_D reduces significantly with an increase in grid resolution. The percentage difference of C_L/C_D values of the coarse and medium mesh is 2.89%, whereas, for the medium and fine mesh, the difference is 0.078%. Likewise, the variations between the results of the fine and very fine grid are also marginal ($3.25 \cdot 10^{-5}$%).

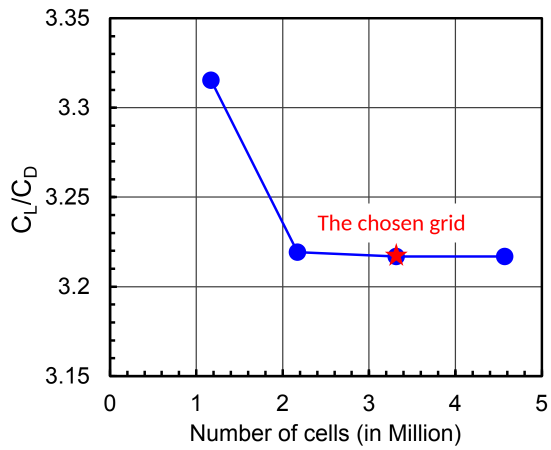

Fig. 14 Comparison of C_L/C_D values at AOA = 20 deg for various grids.

As a trade-off between the accuracy and the computational time, the fine grid is used for the numerical simulations presented in this paper.

B. Convergence Study – Residuals and Forces

The residuals of the pressure, velocity, and other turbulence quantities such as k and ω are monitored to verify the convergence criteria of the present simulations. The numerical accuracy statement of the ASME Journal of Fluids recommended a convergence criteria value lower than 10^{-4} [91]; however, in the present study, a tighter convergence value of 10^{-6} is used for the simulations. Fig.15 displays the evolution of residuals for the UCAV model at 20 and 35 deg AOA. As shown in the figure, at 20 deg AOA, the residual of all variables reaches a value less than 10^{-5} after 1000 iterations whereas, for 35 deg case, it happens after 1600 iterations. Generally, the residuals take a longer time to converge with an increase in AOA owing to modified flow behaviour such as flow separation, vortex breakdown etc. Fig.16 displays the evolution of non-dimensional L/D ratio for 20 and 35 deg at Ma = 0.087 and the evolution of the L/D ratio for 15 and 20 deg at Ma = 0.8. It can be observed that the forces converge after approximately 500 iterations for both cases. Furthermore, all simulations were run up to 3000 iterations to minimize the iteration convergence error.

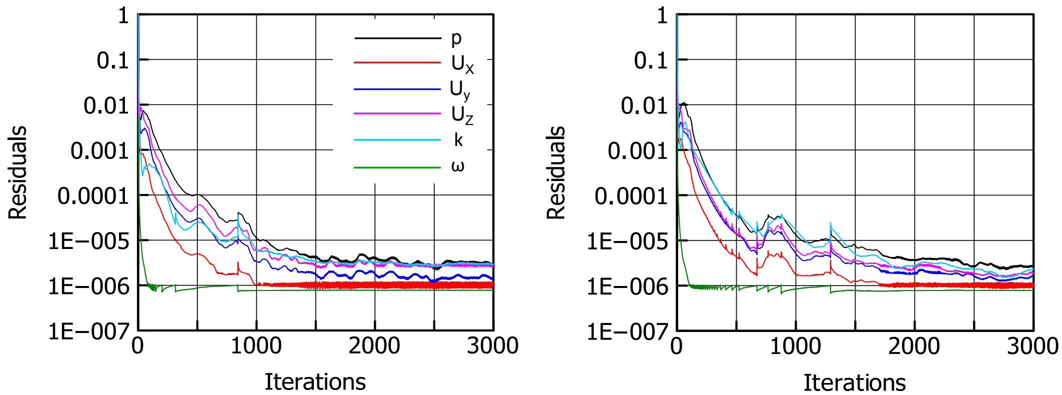

Fig. 15 Evolution of residuals for the UCAV model at 20 and 35 deg AOA, Ma = 0.087.

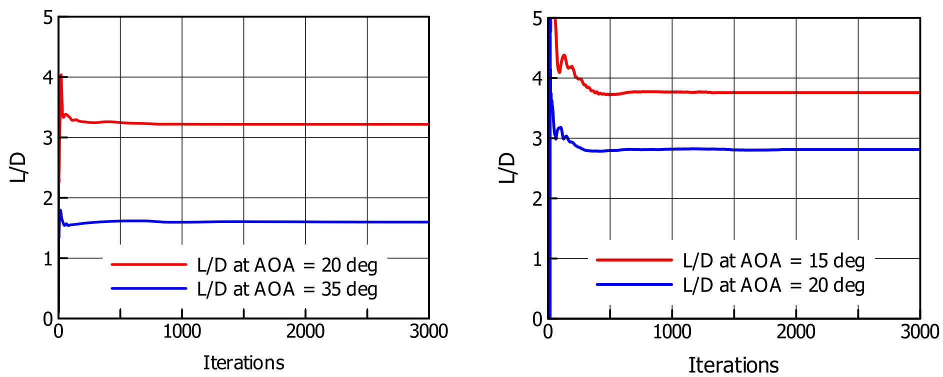

Fig. 16 Evolution of L/D values for the UCAV model for 20 and 35 deg at Ma = 0.087 (left) and for 15 and 20 deg at Ma = 0.8 (right).

C. Validation of the Numerical Approach

The numerical results need a proper validation study to guarantee the accuracy of the numerical model used. Generally, the numerical results are compared with experimental or analytical results for validation. As the current UCAV model lacks experimental results at the moment, for validation, the generic lambda wing models at the low speed [21] and SACCON, DLR-F17E models at high speed [50] are compared with their corresponding experimental results following the same numerical approach adapted for the present UCAV model. As shown in (Fig.17) and (Fig.18), the numerical models satisfactorily predict the lift and drag characteristics of the generic lambda wings and SACCON, DLR-F17E for Ma = 0.087 and Ma = 0.8 regimes considered in this study. For the present UCAV wing, the numerical model with identical mesh, boundary conditions, numerical scheme, etc., is used to improve the reliability of the present numerical results. Lastly, it can be concluded that the present numerical models are adequate to investigate the aerodynamic characteristics of the UCAV model at low and high speeds.

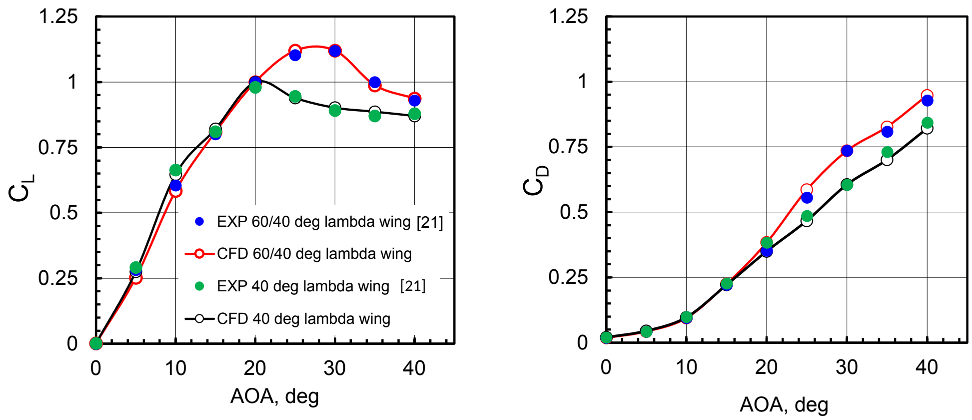

Fig. 17 Validation of CFD with Experimental data, Ma = 0.087.

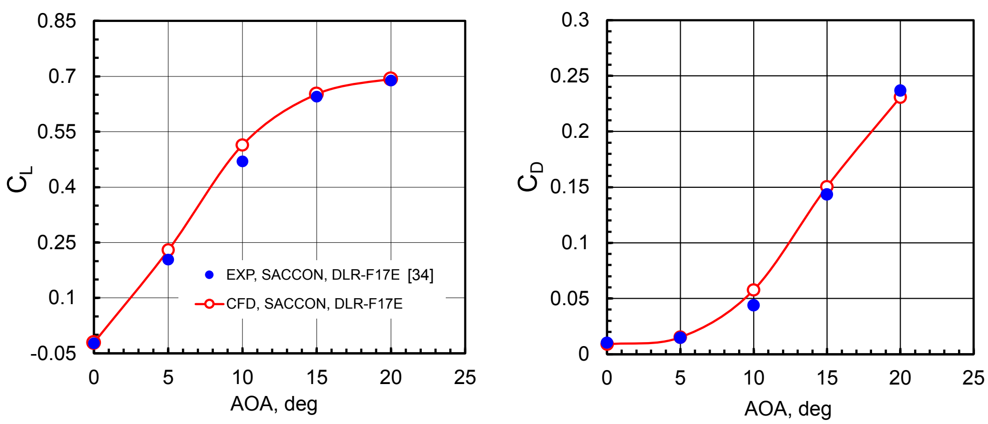

Fig. 18 Validation of CFD with Experimental data, Ma = 0.8.

D. Aerodynamic Characteristics of the Model

The aerodynamic characteristics of the baseline and the optimized UCAV models at low-speed (Ma = 0.087) are provided in Fig.19. As shown in the figure, the optimized model exhibits a minor improvement in the lift and drag values for the full flow range. Furthermore, the effect of the inlet lip on the optimized model for the low and high Mach numbers are provided in Fig.20, 21 and 22, respectively. It was found that the presence of inlet lip adversely affects the lift values in both cases. However, this effect is more pronounced for the low-speed case compared to the high-speed case due to a low CR value of the lip geometry. Moreover, Fig.22 compares the C_p distribution on the SS for the model with and without inlet lip integration for 15 deg, AOA. As shown in Fig.22, the C_p distribution is almost identical for both configurations, excluding the lip zone, where the pressure is different. Because of this reason, the effect of the lip is not very severe on the aerodynamic performance.

Our research group plans to study experimentally and numerically the aerodynamic characteristics of a non-constant

LE-swept UCAV model without the effect of the embedding inlet lip. For this reason, in this paper, flowfield analyses do not consider the impact of the embedding inlet lip on the aerodynamic characteristics of the present UCAVs.

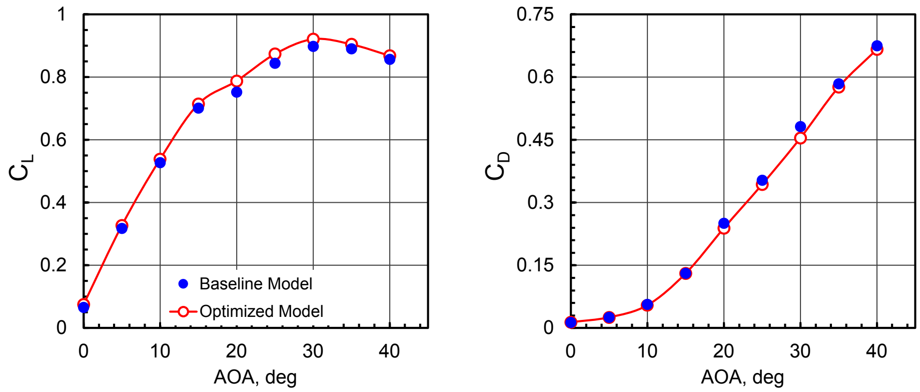

Fig. 19 Aerodynamic characteristics of the UCAV model at low speed, Ma = 0.087.

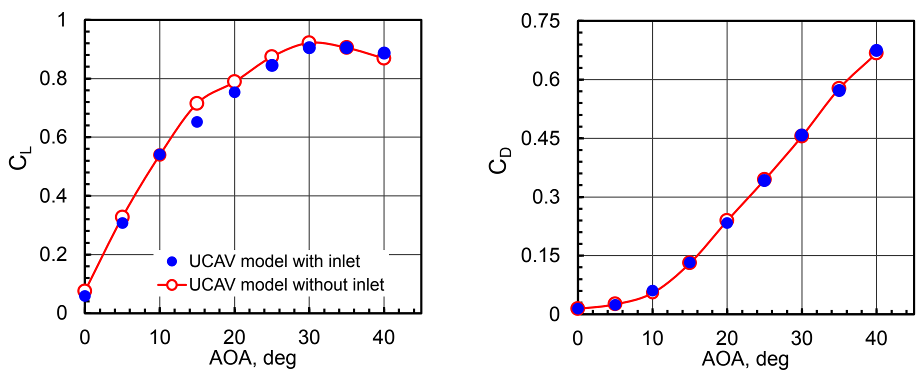

Fig. 20 Aerodynamic characteristics of the UCAV model with and without inlet at low speed, Ma = 0.087.

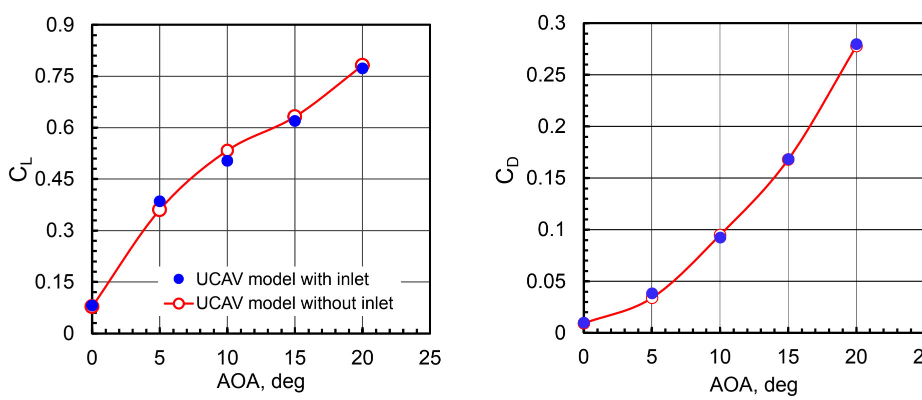

Fig. 21 Aerodynamic characteristics of the UCAV model with and without inlet at high speed, Ma = 0.75.

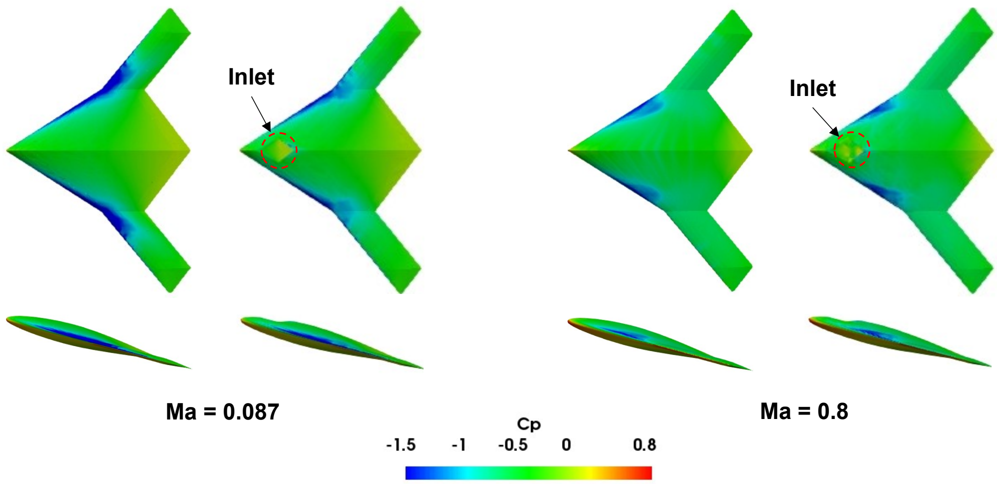

Fig. 22 C_p distribution of the UCAV model with and without inlet lip at 15 deg.

E. Flowfield Analyses

The coefficient of pressure (C_p) distribution at the symmetry plane for the UCAV model (without inlet) at various AOA (15 to 40 deg) is shown in Fig.23. A stagnation zone is visible on the pressure surface (PS) of the LE for all cases, and its size increases with the increase in the AOA. A low-pressure area is observed on the SS, and it indicates the vortex that is generated on the SS. It expands with an increase in AOA, and it engulfs the SS, and this effect is more pronounced for AOA values greater than 25 deg.

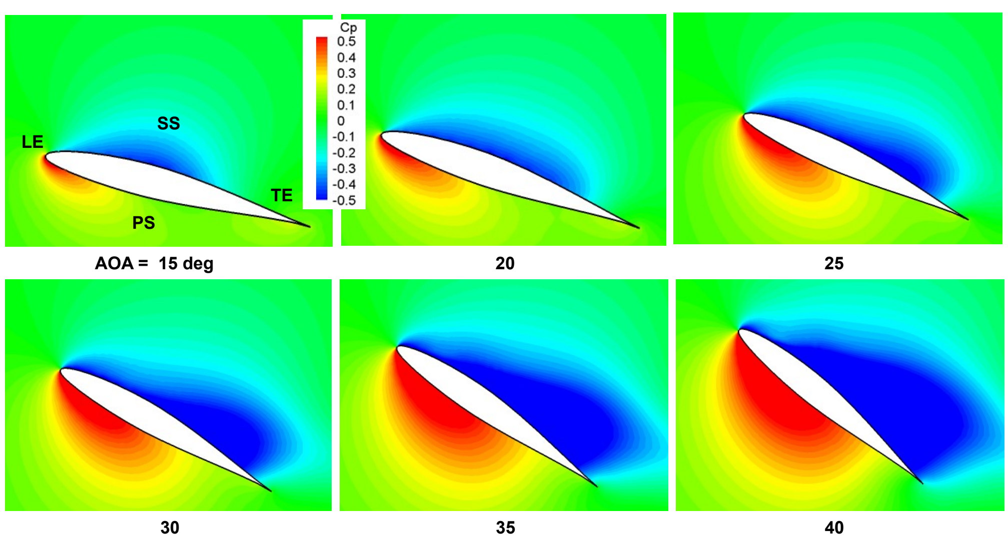

Fig. 23 Cp distribution at the symmetry plane for the UCAV model, Ma = 0.087.

To elucidate the evolution of vortical flow structures at low-speed, the Cp distribution at the SS with surface streamlines for various AOA (0 to 40 deg with a step of 5 deg) values is provided in Fig.24. The high-pressure distribution on most SS at AOA = 0 deg decreases over LE regions when AOA increases to 5 deg and 10 deg. At 15 deg

AOA, two dominant vortices, such as wing and strake vortex, were observed clearly. The vortical structures expanded and weakened in strength, and they shifted from outboard to inboard of the wing with increasing AOA. Furthermore, the increased radius of the surface streamlines indicates the expansion of the vortex core, and the vortex elongates with the AOA. Additionally, the UCAV wing model displays a stable vortex even at higher AOA, and the stall inception was delayed. This delayed stall phenomenon can be attributed to the effect of highly swept non-constant LE.

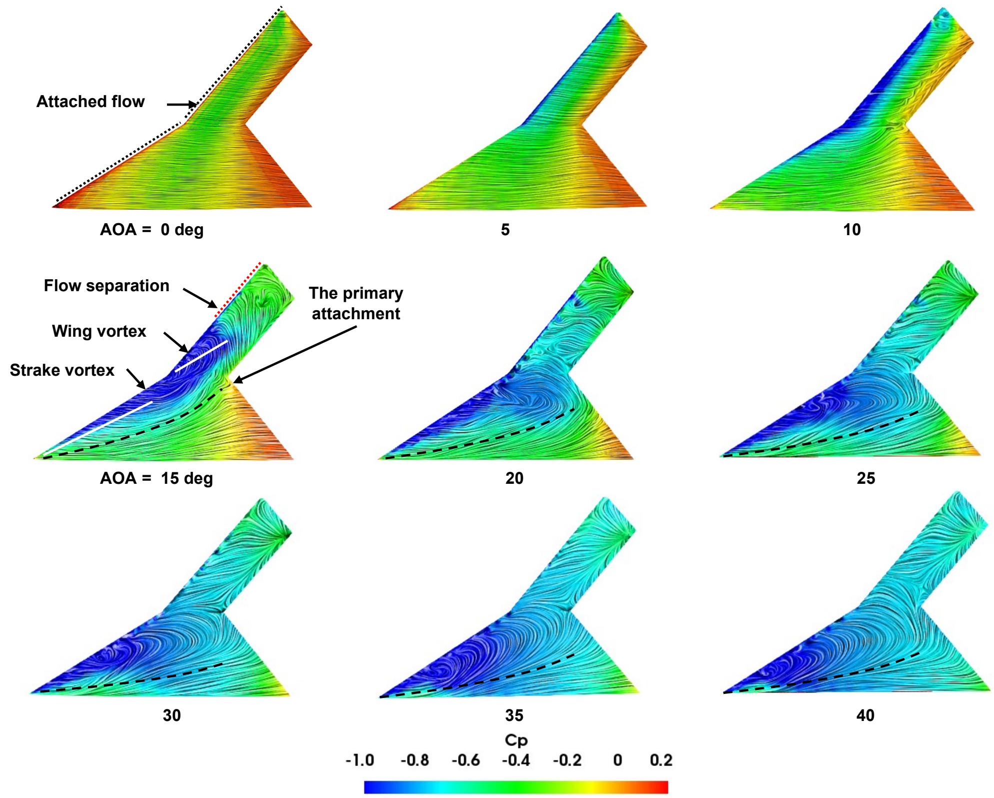

Fig. 24 Cp contour with wall shear streamlines for the UCAV mode, Ma = 0.087.

Fig.25 provides the isosurface of Lambda 2 criterion at value 30000 to display the vortical structures. At 15 deg AOA, the flow on the wing outboard separates, and the separation region increases as it moves inboard with the increase in AOA. It can also be noticed that the separated vortex shows reduced intensity as size increases with increasing AOA. For AOA > 20 deg, flow separation reaches the inboard section, and its size increases gradually with AOA. Due to the presence of the strake in the non-constant LE sweep angle configuration, the flow is attached to the central plane and exhibits higher velocity near LE.

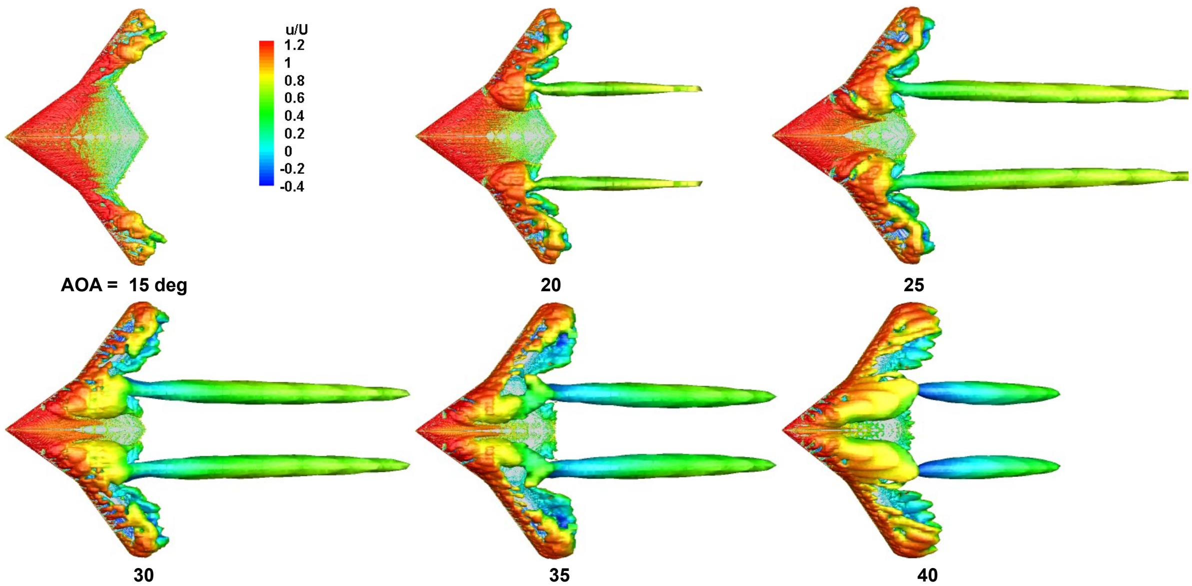

Fig. 25 The iso-surface of Lambda 2 criterion (=30000), Ma = 0.087.

Fig.26 shows the SS Cp distribution with surface streamlines for various AOA (0 to 20 deg with the step of 5 deg) at high speed, M = 0.80. At AOA = 0 deg, high pressure occurs over most of the SS. With an increase in AOA to 5 deg, shock-induced flow separation occurs due to a higher free stream Ma number (=0.8). As AOA increases from 10 to 20 deg, flow separation is visible over the outboard section, whereas a strake vortex is observed clearly. Furthermore, the surface streamlines show the expansion of the strake vortex core with the increase in AOA.

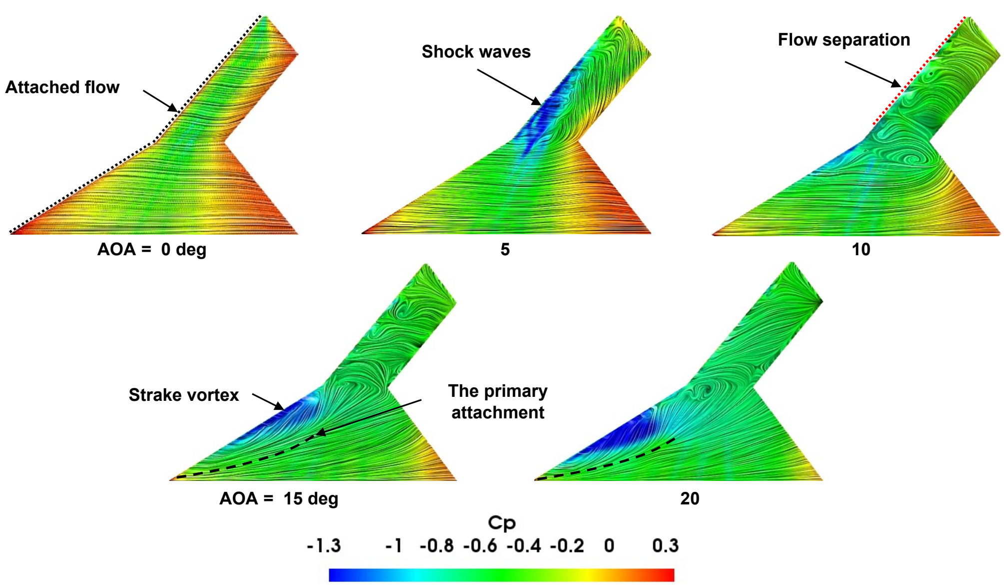

Fig. 26 Cp contour with wall shear streamlines for the UCAV mode, Ma = 0.8.

Fig.27 shows Mach number and C_p distribution at various spanwise slices for high-speed case (Ma = 0.8). As shown in Fig.27 a, the plane slices 1 to 4 are created along the wingspan to display the Mach number (Fig.27 b) and C_p distribution (Fig.27 c). The plan slices reveal several shock waves on the SS of the wing. Furthermore, a local supersonic flow field and the first shock wave are visible closer to the LE, and additional shock waves can be noticed downstream of the first shockwave which leads to the shock-induced separation.

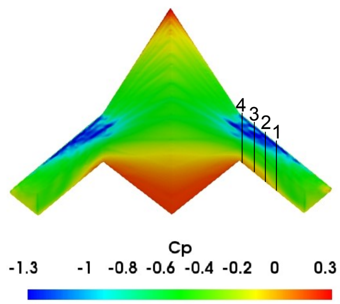

a) SS Cp distribution at Ma = 0.8

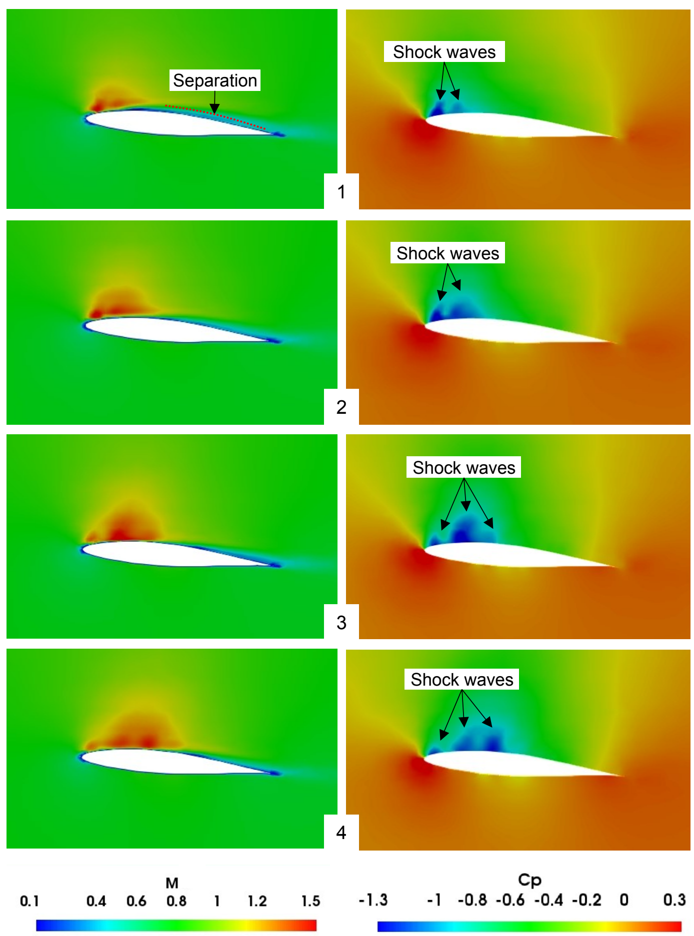

b) Ma distribution **c) Cp distribution**

Fig. 27 Various two-dimensional spanwise planes with Ma number contours and C_p distribution at AOA = 5 deg.

VI. Conclusion

The present work discusses the conceptual design of a tailless flying wing using multi-fidelity analysis such as the vortex lattice method and CFD to enhance the aerodynamic characteristics. The present conceptual design study begins with the initial sizing step, which considers the critical parameters such as thrust-to-takeoff weight ratio, total fuel weight fraction, payload, and empty weight. Later, an estimate for the planform area was provided in the aerodynamic sizing stage. Lastly, the conceptual design phase involves the planform with and without embedding an inlet lip, and a non-constant LE sweep angle configuration was adopted owing to their better lift and drag characteristics.

Our research team plans to perform some experimental studies at the University of Glasgow De Havilland Wind Tunnel in the next phase of the project to investigate the aerodynamic characteristics of non-constant LE swept UCAVs and to validate computational results. For this reason, based on the obtained conceptual design, a 1:20 scaled-down UCAV model design is generated to be used in the experiments later. Before manufacturing the experimental UCAV model, a preliminary design optimization study is performed to improve the scaled-down UCAV model for the flight conditions implied by the wind tunnel. The sweep angles of the conceptual design configuration were optimized using the low-fidelity vortex lattice method and the Kriging surrogate model to save computational time. The vortex lattice method is computationally inexpensive and suitable for the present preliminary design optimization process. Later, the optimized design point was investigated by solving high-fidelity Reynolds-averaged Navier-Stokes equations using an open-source CFD code, OpenFOAM 8.0. The aerodynamic characteristics of the optimized design were analyzed by plotting surface streamlines, Lambda2 criterion, pressure distribution etc. The aerodynamic behavior and flowfield of the UCAV configuration with and without embedding inlet lip have been assessed at low and high speeds. It was found that the inlet lip produced a minor decrement in C_L values, and the C_p distribution was identical to with and without inlet lip case with local changes near the lip region.

Additionally, the present investigation serves as a foundation for planned experimental studies on the baseline configuration and flow control methods for the UCAV concept. In future studies, we aim to implement non-planar lifting surfaces into the UCAV concept and perform more advanced optimization studies followed by the experimental studies to develop the concept.

Acknowledgments

The authors would like to acknowledge NATO STO Support Project AVT-SP-002 Turbulence and the Aerodynamic Optimization of Nonplanar Lifting Systems.

References

[1] House of Commons Defence Committee, U. K., "The contribution of Unmanned Aerial Vehicles to ISTAR capability," *The Stationery Office Limited, London*, 2008. URL https://publications.parliament.uk/pa/cm200708/cmselect/

cmdfence/1087/1087.pdf.

[2] Austin, R., *Unmanned aircraft systems: UAVS design, development and deployment*, John Wiley & Sons, 2011.

[3] Hitzel, S. M., "Flightphysical aspects and methods of future military aircraft designs," *Paper presented* 5^{th} *Challenges in European Aerospace CEAS Air & Space Conference*, 2015, pp. 1–25. URL https://aerospace-europe.eu/media/books/CEAS2015_119.pdf.

[4] Haulman, D. L., "US unmanned aerial vehicles in combat, 1991-2003," Tech. rep., Air force historical research agency Maxwell AFB AL, 2003. URL https://apps.dtic.mil/sti/citations/ADA434033.

[5] Gundlach, J., *Designing unmanned aircraft systems: a comprehensive approach*, American Institute of Aeronautics and Astronautics, 2012.

[6] Ganglin, W., "Key parameters and conceptual configuration of unmanned combat aerial vehicle concept," *Chinese Journal of Aeronautics*, Vol. 22, No. 4, 2009, pp. 393–400. https://doi.org/https://doi.org/10.1016/S1000-9361(08)60116-8.

[7] Florance, J., Fleming, G., Burner, A., Graves, S., Hunter, C., Martin, C., and Scherer, L., "Contributions of the NASA Langley Research Center to the DARPA/AFRL/NASA/Northrop Grumman smart wing program," 44^{th} *AIAA/ASME/ASCE/AHS/ASC structures, structural dynamics, and materials conference, Norfolk, Virginia, 07- 10 April 2003*, AIAA Paper 2003-1961. https://doi.org/https://doi.org/10.2514/6.2003-1961.

[8] Cummings, R. M., and Schütte, A., "The NATO STO Task Group AVT-201 on 'Extended Assessment of Stability and Control Prediction Methods for NATO Air Vehicles," 32^{nd} *AIAA Applied Aerodynamics Conference, Atlanta, GA, 16-20 June 2014*, AIAA Paper 2014-2000, p. 2000. https://doi.org/https://doi.org/10.2514/6.2014-2000.

[9] McParlin, S., Bruce, R., Hepworth, A., and Rae, A., "Low speed wind tunnel tests on the 1303 UCAV concept," 24^{th} *AIAA Applied Aerodynamics Conference, San Francisco, California, 05 June - 08 June 2006*, AIAA Paper 2006-2985, p. 2985. https://doi.org/https://doi.org/10.2514/6.2006-2985.

[10] Petterson, K., "CFD analysis of the low-speed aerodynamic characteristics of a UCAV," 44^{th} *AIAA Aerospace Sciences Meeting and Exhibit, 09 - 12 January 2006, Reno, Nevada*, 2006, AIAA Paper 2006-1259, p. 1259. https://doi.org/https://doi.org/10.2514/6.2006-1259.

[11] Petterson, K., "Low-speed aerodynamic and flowfield characteristics of a UCAV," 24^{th} *Applied Aerodynamics Conference. San Francisco, California 5-8 June*, AIAA Paper 2006-2986. https://doi.org/https://doi.org/10.2514/6.2006-2986.

[12] Woolvin, S., "UCAV configuration & performance trade-offs," 44^{th} *AIAA Aerospace Sciences Meeting and Exhibit, Reno, Nevada, 09 - 12 January, 2006*, AIAA Paper 2006-1264, p. 1264. https://doi.org/https://doi.org/10.2514/6.2006-1264.

[13] Coppin, J., "Aerodynamics, stability and shape optimisation of unmanned combat air vehicles," Ph.D. thesis, University of Sheffield, 2014. URL https://etheses.whiterose.ac.uk/6987/1/thesis-Joe-Coppin.pdf.

[14] Cummings, R., and Schuette, A., "An integrated computational/experimental approach to UCAV stability & control estimation: overview of NATO RTO AVT-161," 28^{th} *AIAA Applied Aerodynamics Conference, Chicago, Illinois, 28 June 2010 - 01 July 2010*, AIAA Paper 2010-4392, p. 4392. https://doi.org/https://doi.org/10.2514/6.2010-4392.

[15] Liersch, C. M., Huber, K. C., Schütte, A., Zimper, D., and Siggel, M., "Multidisciplinary design and aerodynamic assessment of an agile and highly swept aircraft configuration," *CEAS Aeronautical Journal*, Vol. 7, No. 4, 2016, pp. 677–694. https://doi.org/https://doi.org/10.1007/s13272-016-0213-4.

[16] Cummings, R. M., Liersch, C., and Schuette, A., "Multi-disciplinary design and performance assessment of effective, agile NATO air vehicles," *2018 Applied Aerodynamics Conference, Atlanta, Georgia, June 25-29, 2018*, AIAA Paper 2014-2838, June 2018, p. 2838. https://doi.org/https://doi.org/10.2514/6.2018-2838.

[17] Liersch, C. M., Cummings, R., Schütte, A., et al., "NATO STO/AVT-251: A Joint Exercise in Collaborative Combat Aircraft Design," *NATO STO Review*, 2022. https://doi.org/https://review.sto.nato.int/index.php/journal-issues/spring-2022/avt-324/39-a-joint-exercise-in-collaborative-combat-aircraft-design.

[18] Liersch, C. M., and Bishop, G., "Conceptual design of a 53 deg swept flying wing UCAV configuration," *2018 Applied Aerodynamics Conference, Atlanta, Georgia, June 25-29, 2018*, AIAA Paper 2018-2839, p. 2839. https://doi.org/https://doi.org/10.2514/6.2018-2839.

[19] SchütteSch, A., Vormweg, J., Maye, R. G., and Jeans, T., "Aerodynamic shaping design and vortical flow design aspects of a 53 deg swept flying wing configuration," *2018 Applied Aerodynamics Conference, Atlanta, Georgia, June 25-29, 2018*, AIAA Paper 2018-2841, p. 2841. https://doi.org/https://doi.org/10.2514/6.2018-2841.

[20] Nangia, R. K., Coppin, J., and Ghoreyshi, M., "A UCAV Wing Design, Assessment and Comparisons." *2018 Applied Aerodynamics Conference, Atlanta, Georgia, 25-29 June, 2018*, AIAA Paper 2018-2842, p. 2842. https://doi.org/https://doi.org/10.2514/6.2018-2842.

[21] Ali, U., and Chadwick, E., "Flow control and high-lift performance for flying-wing manned Combat Air Vehicle Configurations by inserting lots," *The International Journal of Multiphysics*, Vol. 10, No. 2, 2016. https://doi.org/http://dx.doi.org/10.21152/1750-9548.10.2.117.

[22] Schütte, A., Hummel, D., and Hitzel, S. M., "Flow Physics Analyses of a Generic Unmanned Combat Aerial Vehicle Configuration," *Journal of Aircraft*, Vol. 49, 2012, pp. 1638–1651. https://doi.org/https://doi.org/10.2514/1.C031386.

[23] Cummings, R. M., and Schütte, A., "Integrated computational/experimental approach to unmanned combat air vehicle stability and control estimation," *Journal of Aircraft*, Vol. 49, No. 6, 2012, pp. 1542–1557. https://doi.org/https://doi.org/10.2514/1.C031430.

[24] Shim, H., and Park, S. O., "Low-speed wind-tunnel test results of a BWB-UCAV model," *Procedia Engineering*, Vol. 67, 2013, pp. 50–58. https://doi.org/https://doi.org/10.1016/j.proeng.2013.12.004.

[25] "The Journal of the JAPCC," https://www.japcc.org/journals/journal-edition-32/, 2021.

[26] Cummings, R. M., and Schÿtte, A., "Numerical solutions for the VFE-2 Configuration on Unstructured Grids at USAFA, United States," *Report: Understanding and Modeling Vortical Flows to Improve the Technology Readiness Level for Military Aircraft*, 2009, p. 1.

[27] Young, M. E., Ghoreyshi, M., Jirasek, A., and Cummings, R. M., "Prediction and Validation of Aerodynamic Characteristics for a Generic UCAV Configuration with Trailing-Edge Flaps," 32^{nd} *AIAA Applied Aerodynamics Conference,Atlanta, GA, 16-20 June 2014*, AIAA Paper 2014-2136, p. 2136. https://doi.org/https://doi.org/10.2514/6.2014-2136.

[28] Cummings, R. M., Liersch, C. M., Schütte, A., and Huber, K. C., "Aerodynamics and conceptual design studies on an unmanned combat aerial vehicle configuration," *Journal of Aircraft*, Vol. 55, No. 2, 2018, pp. 454–474. https://doi.org/https://doi.org/10.2514/1.C033808.

[29] Hitzel, S. M., Boelens, O. J., Rooij, M., and Hövelmann, A., "Vortex development on the AVT-183 diamond wing configuration–numerical and experimental findings," *Aerospace Science and Technology*, Vol. 57, 2016, pp. 90–102. https://doi.org/https://doi.org/10.1016/j.ast.2015.12.007.

[30] Frink, N. T., Tomac, M., and Rizzi, A., "Collaborative study of incipient separation on 53°-swept diamond wing," *Aerospace Science and Technology*, Vol. 57, 2016, pp. 76–89. https://doi.org/https://doi.org/10.1016/j.ast.2016.02.019.

[31] Luckring, J. M., Boelens, O. J., Breitsamter, C., Hövelmann, A., Knoth, F., Malloy, D. J., and Deck, S., "Objectives, approach, and scope for the AVT-183 diamond-wing investigations," *Aerospace Science and Technology*, Vol. 57, 2016, pp. 2–17. https://doi.org/https://doi.org/10.1016/j.ast.2016.05.025.

[32] Hövelmann, A., Grawunder, M., Buzica, A., and Breitsamter, C., "AVT-183 diamond wing flow field characteristics Part 2: Experimental analysis of leading-edge vortex formation and progression," *Aerospace Science and Technology*, Vol. 57, 2016, pp. 31–42. https://doi.org/https://doi.org/10.1016/j.ast.2015.12.023.

[33] Frink, N. T., "Stability and Control CFD Investigations of a Generic 53 deg Swept UCAV Configuration," 32^{nd} *AIAA Applied Aerodynamics Conference, Atlanta, GA, 16-20 June 2014*, AIAA Paper 2014-2133, p. 2133. https://doi.org/https://doi.org/10.2514/6.2014-2133.

[34] Huber, K. C., Schütte, A., Rein, M., and Löser, T., "Experimental aerodynamic assessment and evaluation of an agile highly swept aircraft configuration," *CEAS Aeronautical Journal*, Vol. 8, No. 1, 2017, pp. 17–29. https://doi.org/https://doi.org/10.1007/s13272-016-0219-y.

[35] Vicroy, D. D., Huber, K. C., Schütte, A., Rein, M., Irving, J. P., Rigby, G., Löser, T., Hübner, A.-R., and Birch, T. J., "Experimental investigations of a generic swept unmanned combat air vehicle with controls," *Journal of Aircraft*, Vol. 55, No. 2, 2018, pp. 475–501. https://doi.org/https://doi.org/10.2514/1.C033782.

[36] Ghoreyshi, M., Young, M. E., Lofthouse, A. J., Jirásek, A., and Cummings, R. M., "Numerical simulation and reduced-order aerodynamic modeling of a lambda wing configuration," *Journal of Aircraft*, Vol. 55, No. 2, 2018, pp. 549–570. https://doi.org/https://doi.org/10.2514/1.C033776.

[37] Warsop, C., Smith, D. R., and Miller, D., "NATO AVT-239 task group: innovative control effectors for manoeuvring of air vehicles-conclusions and next steps," *AIAA Scitech 2019 Forum*, 2019, p. 0284.

[38] Smith, D. R., and Warsop, C., "Nato avt-239 task group:'innovative control effectors for manoeuvring of air vehicles'–introduction and overview," *AIAA Scitech 2019 Forum*, AIAA Paper 2019-0041, p. 0041. https://doi.org/https://doi.org/10.2514/6.2019-0041.

[39] Rossignol, K.-S., Proskurov, S., Lummer, M., Ewert, R., Delfs, J. W., Kolb, A., and Mancini, S., "Aeroacoustic assessment of low-observable UCAV configurations," 2020.

[40] Rossignol, K.-S., Pott-Pollenske, M., Delfs, J., Kolb, A., and Patrick, Z., "A Novel Test Bed for the Aeroacoustic Investigation of UCAV Configurations with Highly Integrated Propulsion Systems," *28th AIAA/CEAS Aeroacoustics 2022 Conference*, 2022, p. 2856.

[41] Coiro, E., Lefebvre, S., and Ceolato, R., "Infrared Signature Prediction for Low Observable Air Vehicles," *AVT-324 Specialists' Meeting on Multi-disciplinary design approaches and performance assessment of future combat aircraft*, 2020, pp. MP–AVT.

[42] Lindermeir, E., and Rütten, M., "IR-Signature of the MULDICON Configuration determined by the IR-Signature Model MIRA," *2018 Applied Aerodynamics Conference, 2018*, 2018, p. 3166. https://doi.org/https://doi.org/10.2514/6.2018-3166.

[43] Loeser, T., Vicroy, D., and Schütte, A., "SACCON static wind tunnel tests at DNW-NWB and 14 x22 NASA LaRC," $28^{t}h$ *AIAA applied aerodynamics conference, Chicago, Illinois, 28 June 2010 - 01 July 2010*, AIAA Paper 2010-4393, p. 4393. https://doi.org/https://doi.org/10.2514/6.2010-4393.

[44] Vicroy, D., Loeser, T., and Schütte, A., "SACCON dynamic wind tunnel tests at DNW-NWB and 14´ x22´ NASA LaRC," 28^{th} *AIAA Applied Aerodynamics Conference, 2010*, AIAA Paper 2010-4394, p. 4394. https://doi.org/https://doi.org/10.2514/6.2010-4394.

[45] Schütte, A., Hummel, D., and Hitzel, S. M., "Numerical and experimental analyses of the vortical flow around the SACCON configuration," 28^{th} *AIAA Applied Aerodynamics Conference, Chicago, Illinois, 28 June 2010 - 01 July 2010*, AIAA Paper 2010-4690, p. 4690. https://doi.org/https://doi.org/10.2514/6.2010-4690.

[46] Liersch, C. M., and Huber, K. C., "Conceptual design and aerodynamic analyses of a generic UCAV configuration," 32^{nd} *AIAA Applied Aerodynamics Conference, Atlanta, GA, 16-20 June 2014*, AIAA Paper 2014-2001, p. 2001. https://doi.org/https://doi.org/10.2514/6.2014-2001.

[47] Schütte, A., Huber, K. C., and Boelens, O. J., "Static and dynamic numerical simulations of a generic UCAV configuration with and without control devices," 32^{nd} *AIAA Applied Aerodynamics Conference*, 2014, p. 2132.

[48] Kennett, D. J., Hoholis, G., and Badcock, K. J., "Numerical simulation of control surface deflections over a generic UCAV configuration at off-design flow conditions," 32^{nd} *AIAA Applied Aerodynamics Conference, June 2014*, AIAA Paper 2014-2134, p. 2134. https://doi.org/https://doi.org/10.2514/6.2014-2134.

[49] Tormalm, M., Le Roy, J.-F., and Morgand, S., "Numerical assessment of leading-and trailing-edge control on a swept lambda wing," *Journal of Aircraft*, Vol. 55, No. 2, 2018, pp. 603–622. https://doi.org/https://doi.org/10.2514/1.C033820.

[50] Löchert, P., Huber, K. C., Ghoreyshi, M., and Allen, J., "Control device effectiveness studies of a 53 swept flying wing configuration. Experimental, computational, and modeling considerations," *Aerospace Science and Technology*, Vol. 93, 2019, p. 105319. https://doi.org/https://doi.org/10.1016/j.ast.2019.105319.

[51] Sadraey, M. H., *Aircraft design: A systems engineering approach*, John Wiley & Sons, 2012.

[52] Luckring, J. M., and Boelens, O. J., "A reduced-complexity investigation of blunt leading-edge separation motivated by UCAV aerodynamics," 53^{rd} *AIAA Aerospace Sciences Meeting, Kissimmee, Florida, 5-9 January 2015*, AIAA Paper 2015-0061, p. 0061. https://doi.org/https://doi.org/10.2514/6.2015-0061.

[53] Manshadi, M. D., Eilbeigi, M., Sobhani, M. K., Zadeh, M. B., and Vaziry, M. A., "Experimental study of flow field distribution over a generic cranked double delta wing," *Chinese Journal of Aeronautics*, Vol. 29, No. 5, 2016, pp. 1196–1204. https://doi.org/https://doi.org/10.1016/j.cja.2016.08.002.

[54] Yaniktepe, B., Ö Zalp, C., and Canpolat, Ç., "Aerodynamics and flow characteristics of X-45 delta wing planform," *Kahramanmaraş Sütçü İmam Üniversitesi Mühendislik Bilimleri Dergisi*, Vol. 19, No. 1, 2016, pp. 1–10. https://doi.org/http://jes.ksu.edu.tr/tr/download/article-file/181023.

[55] Kundu, A. K., *Aircraft design*, Vol. 27, Cambridge University Press, 2010.

[56] Sepulveda, E., and Smith, H., "Technology challenges of stealth unmanned combat aerial vehicles," *The Aeronautical Journal*, Vol. 121, No. 1243, 2017, pp. 1261–1295. https://doi.org/10.1017/aer.2017.53.

[57] Valavanis, K. P., and Vachtsevanos, G. J., *Handbook of unmanned aerial vehicles*, Vol. 1, Springer, 2015.

[58] Raymer, D., *Aircraft design: a conceptual approach*, American Institute of Aeronautics and Astronautics, Inc., 2012.

[59] Panahi, A., Zanjani, M. V., Yousefi, S., Fazli, N., and Aarabi, J., "Derivation of structural weight estimation for Unmanned Combat Aerial Vehicle (UCAV)," *The Aeronautical Journal*, Vol. 126, No. 1299, 2022, pp. 813–829. https://doi.org/10.1017/aer.2021.104.

[60] "Northrop Grumman," https://www.northropgrumman.com/wp-content/uploads/UCAS-D_Data_Sheet.pdf, 2015.

[61] "National museum of the United States air force," https://www.nationalmuseum.af.mil/Visit/Museum-Exhibits/Fact-Sheets/Display/Article/196732/boeing-x-45a-j-ucas/, 2015.

[62] Sullivan, M., Clark, J., Matt, L., Keener, K., Masters, T., Chaplain, C., Chin, L., Swierczek, B., and Rambus, M.-A., "Defense Acquisitions: Matching Resources with Requirements Is Key to the Unmanned Combat Air Vehicle Programs Success," Tech. rep., Government Accountability Office WASHINGTON DC United States, 2003.

[63] Palacios, E. S., and Smith, H., "Impact of mission requirements on the design of low observable UCAV configurations," *Aircraft Engineering and Aerospace Technology*, Vol. 91, No. 10, 2019, pp. 1295–1307. https://doi.org/https://doi.org/10.1108/AEAT-09-2018-0249.

[64] Anderson, J. D., *Aircraft performance and design*, Vol. 1, WCB/McGraw-Hill Boston, 1999.

[65] Anderson, J. D., *Fundamentals of aerodynamics*, Vol. 1, McGraw-Hill, 2011.

[66] Nangia, R., and Palmer, M., "A comparative study of UCAV type wing planforms-aero performance & stability considerations," 23^{rd} *AIAA Applied Aerodynamics Conference, Toronto, Ontario, Canada, 06-09 June 2005*, AIAA Paper 2005-5078, p. 5078. https://doi.org/https://doi.org/10.2514/6.2005-5078.

[67] Luers, A. S., "Flow control techniques in a serpentine inlet: an enabling technology to increase the military viability of unmanned air vehicles," Ph.D. thesis, Massachusetts Institute of Technology, 2003. https://doi.org/https://dspace.mit.edu/handle/1721.1/82780.

[68] Tresoldi, A., "CFD Modeling and Analysis of a Boundary Layer Ingesting S-shaped Intake," , 2020. https://doi.org/https://thesis.unipd.it/handle/20.500.12608/21114.

[69] Freuler, P. N., "Boundary layer ingesting inlet design for a silent aircraft," Ph.D. thesis, Massachusetts Institute of Technology, 2005. https://doi.org/https://dspace.mit.edu/handle/1721.1/28903.

[70] Baals, D. D., Smith, N. F., and Wright, J. B., "The development and application of high-critical-speed nose inlets," Tech. rep., National Aeronautics and Space Admin Langley Research Center Hampton VA, 1945. https://doi.org/https://ntrs.nasa.gov/citations/19930091984.

[71] Nichols, M. R., and Keith Jr, A. L., "Investigation of a Systematic Group of NACA 1-Series Cowlings with and without Spinners," Tech. rep., 1949. https://doi.org/https://ntrs.nasa.gov/citations/19930092014.

[72] Baumgardner, D., Huebert, B., and Wilson, C., "Meeting review: Airborne aerosol inlet workshop," Tech. rep., 1991. https://doi.org/https://ntrs.nasa.gov/citations/19920008175.

[73] Zeng, L., Pan, D., Ye, S., and Shao, X., "A fast multiobjective optimization approach to S-duct scoop inlets design with both inflow and outflow," *Proceedings of the Institution of Mechanical Engineers, Part G: Journal of Aerospace Engineering*, Vol. 233, No. 9, 2019, pp. 3381–3394. https://doi.org/https://doi.org/10.1177/0954410018795806.

[74] Re, R. J., "An investigation of several NACA 1-series inlets at Mach numbers from 0.4 to 1.29 for mass flow ratios near 1.0," Tech. rep., 1975. https://doi.org/https://ntrs.nasa.gov/citations/19760007996.

[75] Re, R. J., and Abeyounis, W. K., "A wind tunnel investigation of three NACA 1-series inlets at Mach numbers up to 0.92," Tech. rep., 1996. https://doi.org/https://ntrs.nasa.gov/citations/19970010380.

[76] Albers, J. A., and Miller, B. A., "Effect of subsonic inlet lip geometry on predicted surface and flow Mach number distributions," Tech. rep., 1973. https://doi.org/https://ntrs.nasa.gov/citations/19740003699.

[77] "pymoo," https://pymoo.org/, 2022.

[78] McDonald, R. A., and Gloudemans, J. R., "Open vehicle sketch pad: An open source parametric geometry and analysis tool for conceptual aircraft design," *AIAA SciTech 2022 Forum*, 2022, p. 0004. https://doi.org/https://doi.org/10.2514/6.2022-0004.

[79] "OpenVSP, OpenVSP is a parametric aircraft geometry tool," OpenVSP,OpenVSPisaparametricaircraftgeometrytool,http://openvsp.org/,2021, 2021.

[80] McKay, M. D., Beckman, R. J., and Conover, W. J., "A comparison of three methods for selecting values of input variables in the analysis of output from a computer code," *Technometrics*, Vol. 42, No. 1, 2000, pp. 55–61.

[81] Deb, K., and Pratap, A., "Agarwal and T," *Meyarivan,"A Fast and Elitist Multiobjective Genetic Algorithm: NSGA-II", IEEE_J_EVC*, 2002, pp. 192–197.

[82] "openfoam," https://www.openfoam.com/, 2020.

[83] "solidworks," https://www.solidworks.com/, 2020.

[84] Greenshields, C. J., "OpenFOAM user guide Version 8," *The OpenFOAM Foundation*, Vol. 237, 2020.

[85] Segui, M., Abel, F. R., Botez, R. M., and Ceruti, A., "High-fidelity aerodynamic modeling of an aircraft using OpenFoam–application on the CRJ700," *The Aeronautical Journal*, Vol. 126, No. 1298, 2022, pp. 585–606. https://doi.org/doi:10.1017/aer.2021.86.

[86] Al-Garni, A., and Saeed, F., "Experimental and Numerical Investigation of 65-deg Delta and 65/40-deg Double-Delta Wings in Sideslip," 28^{th} *AIAA Applied Aerodynamics Conference, Chicago, Illinois, 28 June - 01 July 2010*, AIAA Paper 2013-4950, p. 4950. https://doi.org/https://doi.org/10.2514/6.2010-4950.

[87] Brett, J., and Ooi, A., "Effect of sweep angle on the vortical flow over delta wings at an angle of attack of 10," *Journal of Engineering Science and Technology*, Vol. 9, No. 6, 2014, pp. 768–781. URL https://jestec.taylors.edu.my/Vol%209%20Issue%206%20December%2014/Volume%20(9)%20Issue%20(6)%20768-781.pdf.

[88] Zimper, D., and Rein, M., "Experimental and numerical analysis of the transonic vortical flow over a generic lambda wing configuration," 32^{nd} *AIAA Applied Aerodynamics Conference, Atlanta, GA, 16-20 June 2014*, AIAA Paper 2014-2005, p. 2005. https://doi.org/https://doi.org/10.2514/6.2014-2005.

[89] Ko, A., Chang, K., Sheen, D.-J., Jo, Y.-H., and Shim, H. J., "CFD Analysis of the Sideslip Angle Effect around a BWB Type Configuration," *International Journal of Aerospace Engineering*, Vol. 2019, 2019. https://doi.org/https://doi.org/10.1155/2019/4959265.

[90] Kelayeh, R. K., and Djavareshkian, M. H., "Aerodynamic investigation of twist angle variation based on wing smarting for a flying wing," *Chinese Journal of Aeronautics*, Vol. 34, issue 2, No. 2, 2021, pp. 201–216. https://doi.org/https://doi.org/10.1016/j.cja.2020.06.022.

[91] Roache, P. J., Ghia, K. N., and White, F. M., “Editorial policy statement on the control of numerical accuracy,” *Journal of Fluids Engineering*, Vol. 108, No. 1, 1986, p. 2. https://doi.org/https://doi.org/10.1115/1.3242537.